Sill stacking in subseafloor unconsolidated sediments and control on sustained hydrothermal systems: evidence from IODP drilling in the Guaymas Basin, Gulf of California

Christophe Yann Galerne[1], Alban Cheviet[2], Wolf-Achim Kahl[1], Christin Wiggers[1], Wolfgang Bach[1], Florian Neumann[3], Martine Buatier[4], Tobias W Höfig[5], Daniel Lizarralde[6], Andreas Teske[7], Manet Peña Salinas[8], Jens Karstens[9], Christoph Böttner[10], Christian Berndt[9], Ivano W Aiello[11], Kathleen Marsaglia[12], Swanne Gontharet[13], Henning Kuhnert[14], Joann M. Stock[15], Raquel Negrete-Aranda[16], Junli Zhang[1], and Achim J. Kopf[1]

[1]University of Bremen
[2]Université de Franche-Comté
[3]GFZ, German Research Centre for Geosciences
[4]UFR Sciences, Universite de Franche Comte
[5]International Ocean Discovery Program
[6]Woods Hole Oceanographic Institution
[7]University of North Carolina at Chapel Hill
[8]UABC
[9]GEOMAR Helmholtz Centre for Ocean Research Kiel
[10]Christian-Albrechts-Universitat zu Kiel
[11]Moss Landing Marine Laboratories
[12]California State University, Northridge
[13]Sorbonne Université
[14]MARUM - Center for Marine Environmental Sciences, University of Bremen
[15]California Institute of Technology
[16]Centro de Investigacion Cientifica y de Educacion Superior de Ensenada

August 29, 2024

Abstract

Magma emplacement in the top unconsolidated sediments of rift basins is poorly constrained in terms of mechanics and associated hydrothermal activity. Our study compares two shallow sills from the Guaymas Basin (Gulf of California) using core data and analyses from IODP Expedition 385, and high-resolution 2D seismic data. We show that magma stalling in the top uncemented sediment layer is controlled by the transition from siliceous claystone to uncemented silica-rich sediment, promoting flat sill formation. Space is created through a combination of viscous indentation, magma-sediment mingling and fluidization processes. In low magma input regions, sills form above the opal-A/CT diagenetic barrier, while high magma input leads to upward stacking of sills, forming funnel-shaped intrusions near the seafloor. Our petrophysical, petrographic, and textural analyses show that magma-sediment mingling creates significant porosity (up to 20%) through thermal cracking of the assimilated sediment. Stable isotope data of carbonate precipitates indicate formation temperatures of 70-90°C, consistent with the current background geothermal gradient at 250-325 m depth. The unconsolidated, water-rich host sediments produce little thermogenic gas through contact metamorphism, but deep diagenetically formed gas bypasses the low-permeability top sediments via hydrothermal fluids flowing through the magma plumbing system. This hydrothermal system provides a steady supply of hydrocarbons at temperatures amendable for microbial life, acting as a major microbial incubator. Similar hydrothermal systems are expected to be abundant in magma-rich young rift basins and play a key role in sustaining subseafloor ecosystems.

Hosted file

`Galerne et al_Manuscript_23-08-2024.docx` available at https://authorea.com/users/822997/articles/1220080-sill-stacking-in-subseafloor-unconsolidated-sediments-and-control-on-sustained-hydrothermal-systems-evidence-from-iodp-drilling-in-the-guaymas-basin-gulf-of-california

Hosted file

`SI_1_GalerneXal_2024.docx` available at https://authorea.com/users/822997/articles/1220080-sill-stacking-in-subseafloor-unconsolidated-sediments-and-control-on-sustained-hydrothermal-systems-evidence-from-iodp-drilling-in-the-guaymas-basin-gulf-of-california

Hosted file

`SI_2_GalerneXal_2024.docx` available at https://authorea.com/users/822997/articles/1220080-sill-stacking-in-subseafloor-unconsolidated-sediments-and-control-on-sustained-hydrothermal-systems-evidence-from-iodp-drilling-in-the-guaymas-basin-gulf-of-california

Hosted file

`SI_3_GalerneXal_2024.docx` available at https://authorea.com/users/822997/articles/1220080-sill-stacking-in-subseafloor-unconsolidated-sediments-and-control-on-sustained-hydrothermal-systems-evidence-from-iodp-drilling-in-the-guaymas-basin-gulf-of-california

Hosted file

`SI_4_GalerneXal_2024.docx` available at https://authorea.com/users/822997/articles/1220080-sill-stacking-in-subseafloor-unconsolidated-sediments-and-control-on-sustained-hydrothermal-systems-evidence-from-iodp-drilling-in-the-guaymas-basin-gulf-of-california

Hosted file

`SI_5_GalerneXal_2024.docx` available at https://authorea.com/users/822997/articles/1220080-sill-stacking-in-subseafloor-unconsolidated-sediments-and-control-on-sustained-hydrothermal-systems-evidence-from-iodp-drilling-in-the-guaymas-basin-gulf-of-california

Hosted file

`SI_6_GalerneXal_2024.docx` available at https://authorea.com/users/822997/articles/1220080-sill-stacking-in-subseafloor-unconsolidated-sediments-and-control-on-sustained-hydrothermal-systems-evidence-from-iodp-drilling-in-the-guaymas-basin-gulf-of-california

Hosted file

`SI_7_GalerneXal_2024.docx` available at https://authorea.com/users/822997/articles/1220080-sill-stacking-in-subseafloor-unconsolidated-sediments-and-control-on-sustained-hydrothermal-systems-evidence-from-iodp-drilling-in-the-guaymas-basin-gulf-of-california

Hosted file

`SI_8_GalerneXal_2024.docx` available at https://authorea.com/users/822997/articles/1220080-sill-stacking-in-subseafloor-unconsolidated-sediments-and-control-on-sustained-hydrothermal-systems-evidence-from-iodp-drilling-in-the-guaymas-basin-gulf-of-california

Title:

Sill stacking in subseafloor unconsolidated sediments and control on sustained hydrothermal systems: evidence from IODP drilling in the Guaymas Basin, Gulf of California

Authors:

Christophe Galerne[1,2,*], Alban Cheviet[2,3], Wolf-Achim Kahl[4], Christin Wiggers[2], Wolfgang Bach[1,2], Florian Neumann[5], Martine Buatier[3], Tobias W. Höfig[6,7], Daniel Lizarralde[8], Andreas Teske[9], Manet Peña-Salinas[10], Jens Karstens[11], Christoph Böttner[12], Christian Berndt[11], Ivano W. Aiello[13], Kathleen M. Marsaglia[14], Swanne Gontharet[15], Henning Kuhnert[1], Joann Stock[16], Raquel Negrete-Aranda[17], Junli Zhang[1], Achim Kopf[1]

[1]MARUM Center for Marine Environmental Sciences, University of Bremen, 28359 Bremen, Germany
[2]FB5 Geosciences, University of Bremen, 28359 Bremen, Germany
[3]Laboratoire Chrono-Environment, UMR 6249, Université Franche-Comté, 25000 Besançon, France
[4]MAPEX - Center for Materials and Processes, University of Bremen, 28359 Bremen, Germany
[5]GFZ, German Research Centre for Geosciences, Section 4.8 Geoenergy, Telegrafenberg, 14473 Potsdam, Germany
[6]International Ocean Discovery Program, Texas A&M University, College Station, TX 77845, USA
[7]Coastal, Marine, and Polar Research, Research Center Jülich, 18069 Rostock, Germany
[8]Department of Geology and Geophysics, Woods Hole Oceanographic Institution, Woods Hole, MA 02543, USA
[9]Department of Earth, Marine and Environmental Sciences, University of North Carolina at Chapel Hill, Chapel Hill, NC 27599, USA
[10]Department of Coastal Oceanography, UABC, Zona Playitas, Ensenada, BC 22860, Mexico
[11]GEOMAR | Helmholtz-Zentrum für Ozeanforschung Kiel, D-24148 Kiel, Germany
[12]Department of Geoscience, Aarhus University, 8000 Aarhus, Denmark
[13]Moss Landing Marine Laboratories, San Jose State University, Moss Landing, CA 95039 USA
[14]Department of Geological Sciences, California State University, Northridge, CA 91330-8266, USA
[15]LOCEAN, UMR 7159, Sorbonne Université/CNRS/IRD/MNHN, 4 place Jussieu, 75252 Paris Cedex 05, France.
[16] Division of Geological and Planetary Sciences, California Institute of Technology, Pasadena CA 91125, USA
[17]Department of Geology, CICESE, Ensenada, BC 22860, Mexico

Key words:

Sill emplacement, Volcanology, Unconsolidated sediments, Peperite, Low-temperature hydrothermal system, IODP Expedition 385

Abstract

Magma emplacement in the top unconsolidated sediments of rift basins is poorly constrained in terms of mechanics and associated hydrothermal activity. Our study compares two shallow sills from the Guaymas Basin (Gulf of California) using core data and analyses from IODP Expedition 385, and high-resolution 2D seismic data. We show that magma stalling in the top uncemented sediment layer is controlled by the transition from siliceous claystone to uncemented silica-rich sediment, promoting flat sill formation. Space is created through a combination of viscous indentation, magma-sediment mingling and fluidization processes. In low magma input regions, sills form above the opal-A/CT diagenetic barrier, while high magma input leads to upward stacking of sills, forming funnel-shaped intrusions near the seafloor. Our petrophysical, petrographic, and textural analyses show that magma-sediment mingling creates significant porosity (up to 20%) through thermal cracking of the assimilated sediment. Stable isotope data of carbonate precipitates indicate formation temperatures of 70−90°C, consistent with the current background geothermal gradient at 250−325 m depth. The unconsolidated, water-rich host sediments produce little thermogenic gas through contact metamorphism, but deep diagenetically formed gas bypasses the low-permeability top sediments via hydrothermal fluids flowing through the magma plumbing system. This hydrothermal system provides a steady supply of hydrocarbons at temperatures amendable for microbial life, acting as a major microbial incubator. Similar hydrothermal systems are expected to be abundant in magma-rich young rift basins and play a key role in sustaining subseafloor ecosystems.

Plane Language Summary

Our study investigates how magma forms sills (sheet-like magma bodies) in soft, wet sediments in the Guaymas Basin, Gulf of California. We analyze core samples from an ocean drilling expedition along with seismic data. We show that when magma moves from hard, siliceous claystone to softer, uncemented silica-rich sediment, it stops ascending and spread horizontally to form sills. Space for these sills, is created by a combination of magma squeezing host sediment and mingling with it. In areas with low magma supply, sills consistently form at a specific depth, just above the boundary between hard and soft sediments. In areas with more frequent magma supply, multiple sills stack up, eventually forming a funnel-shaped sill near the seafloor. We also show that when the magma mingles with the host sediments, it creates significant porosity (vesicles) that nucleates from thermogenic gas liberated by thermal cracking of the organic-rich sediment. This porosity translates into high permeability, allowing hydrothermal fluids to flow through carrying heat and gases from deeply buried sediments. These conditions create stable hydrothermal systems with moderate temperatures (<90°C) where they may play a crucial role in supporting life at, and beneath the seafloor.

1. Introduction

Magma propagation and emplacement into the upper crust require space to accommodate the additional volume. The ability of the host lithology to deform upon the arrival of magma thus controls the shape and orientation of the magma conduit. In basement rocks, fracturing dominates the conduit shape, resulting mostly in discordant dikes that follow regional tectonic stresses, whilst in the emplacement environment where preferred weakness planes are parallel, sheet intrusions form concordant with this main planar anisotropy. In sedimentary basins, this lithological control leads to the formation of horizonal sills, where magma emplacement is accommodated by either uplifting the overburden in a process called forced folding (e.g., Hansen and Cartwright, 2006; Galland et al., 2009; Schmiedel et al., 2017; Galland et al., 2018), or by a process of viscous indentation, where the host lithology is compressed laterally (e.g., Merle and Donnadieu, 2000; Mathieu et al., 2008; Spacapan et al., 2016). A relatively weak sediment layer sandwiched between stiff strata results in flat sill formation (viscous indenter model). A sill emplaced at the interface of sedimentary units of similar strength and stiffness can uplift and bend the overburden. Forced folding is characterized by doming of the free surface (seafloor) that outlines the edge of the sill intrusion at depth (Galland and Scheibert, 2013). Forced folding typically promotes the development of saucer-shaped sills (e.g., Galland et al., 2009; Galerne et al., 2011).

While magma emplacement within deep strata of sedimentary basins is well understood, the mechanism of magma propagation through the uppermost unconsolidated sediments is poorly constrained and difficult to image seismically, since these sediments are often saturated with gas. However, this magma emplacement process is fundamental in understanding how the magma can ultimately erupt at the seafloor through a thick pile of soft sediments, and eventually initiates the formation of volcanic edifices. While geophysical technology fails to provide clear and decisive insight into this process in active geological settings, field geology surveys on exhumed rift systems often exhibit particular magma-sediment facies called peperites (e.g. Galerne et al., 2006), that are indicative of dynamic mingling occurring during magma emplacement (Skilling et al., 2002). Because most of these outcrops are millions of years old, the geological facies are difficult to relate to general magma body geometries and the resulting style of hydrothermal activity it may have been related to. Additionally, peperites represent the final (preserved) mingling textures between magma and sediment that resulted from magma sediment interaction. Despite good general understanding of the various mingling mechanisms (e.g., Skilling et al., 2002; Wohletz, 2002; Zimanowski and Büttner, 2002), the physical and chemical transformations, as well as accurate understanding of heat exchange, and potential role in elemental cycling (e.g. carbon) are poorly constrained.

The Guaymas Basin is a young rift basin in the Gulf of California that displays synchronous processes of sedimentation, tectonics, magmatism and hydrothermalism (e.g. Teske et al., 2021a;

Berndt et al., 2016). The basin is filled with organic-rich sediments deposited at high rates (~1 m/kyr Teske et al., 2021a) that are intruded by large volumes of off-axis sills (Lizarralde et al., 2007; 2011; Berndt et al., 2015; Berndt et al., 2016). The Guaymas Basin thus is a natural field laboratory that enables the investigation of poorly understood magma-propagation processes through the unconsolidated uppermost sediments common to active basins. Some early work based on Deep Sea Drilling Project (DSDP) Leg 64 holes laid the foundation for understanding that sills form as soon as the magma ascent reaches the soft sediment lithology (Einsele et al., 1980; Einsele, 1982; 1985). However, since this pioneering work, no significant advance has been made on the magma emplacement in this context and on the related hydrothermal system.

Sill intrusions in sedimentary basins are known to form concentric rings of hydrothermal vent complexes (HVCs) that root at the edge of sills at depth (e.g. Jamtveit et al., 2004; Berndt et al., 2016; Kjoberg et al., 2017). In the context of this study, the suspected top depth of the sill associated with the Ringvent hydrothermal system, drilled at International Ocean Discovery Program (IODP) Expedition 385 Sites U1547 and U1548 (Teske et al., 2021a), is unusual. It is within less than 80 m from the seafloor, a very shallow depth at which pipes, of only a few tens of meters in length, connect vertically the edge of the sill at depth to vents at the seafloor. Comparable pipe structures imaged off Norway are nearly kilometer-long vertical conduits (e.g. Svensen et al., 2004; Kjoberg et al., 2017). Equally contrasting, the host sediments of the Guaymas Basin are highly porous (70−80%), unconsolidated, and water-saturated (Teske et al., 2021a). Seismic imaging of sill intrusions in this context should be straightforward due to the acoustic impedance contrast between the sill intrusions and the unconsolidated host sediments. However, a set of crossing seismic lines across and around the Ringvent hydrothermal system acquired by two separate campaigns show very complex geometries (Fig. 1).

Our study uses information and material from four IODP sites cored during Expedition 385 (X385). These includes a pair of reference Sites U1545 and U1546 (respectively, Teske et al., 2021b,c, Fig. 1A), that provide insight into the pristine sedimentary column down to 500 mbsf (U1545) and an example of the same sedimentary column intruded recently by a flat massive sill (U1546), respectively (Lizarralde et al., 2023; Cheviet et al., 2023). Our study systematically compares available information from both sites, particularly the cored reference sill (Site U1546, Teske et al., 2021c), and that found underlying the Ringvent area (Sites U1547 and U1548, Teske et al., 2021d). To facilitate the seismic interpretation and clarify the geometry of the sill intrusion at the Ringent site, we integrate petrophysical data from ten IODP X385 holes drilled at and near this location, respectively (Sites U1547 and U1548, Teske et al., 2021d, Fig. 1B). The state of the Ringvent hydrothermal system at present is deduced from *in situ* temperatures obtained from a short temperature probe near the vent mouths at the seafloor, and from IODP X385 downhole temperature measurements (Teske et al., 2019; Teske et al., 2021d; Neumann et al., 2023). The reconstructed thermal field at depth is cross-validated with temperatures derived from oxygen isotope measurements on carbonate precipitated in the voids of the Ringvent sill.

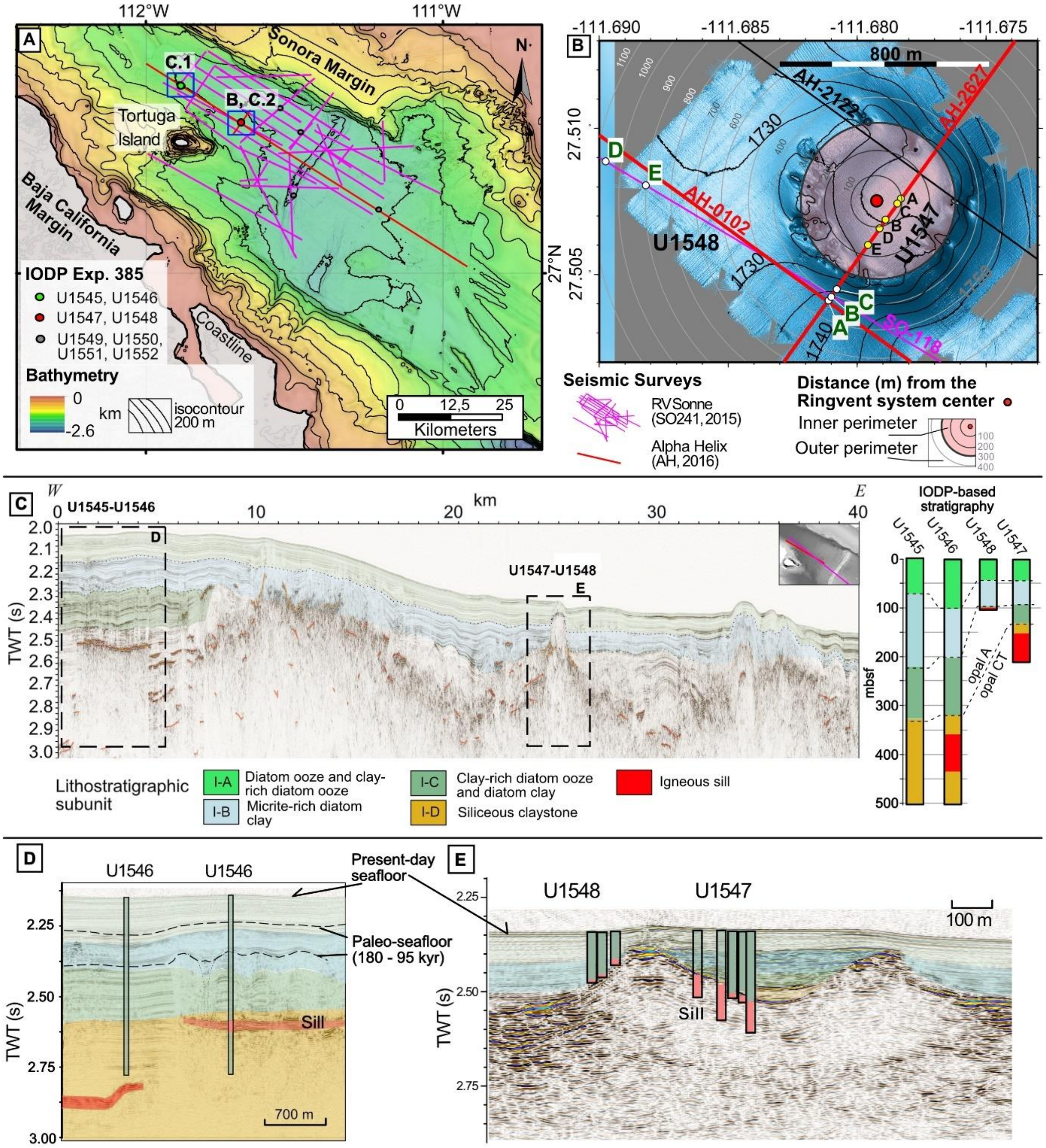

Figure 1. A. Bathymetric map of the Guaymas Basin (Gulf of California) showing the location of the main IODP X385 sites presented in this study and the location of the seismic survey lines used (SO241, AH2016). B. Detailed bathymetric map of the Ringvent area obtained by AUV Sentry (Teske et al., 2019) with IODP X385 sites and seismic lines. An axisymmetric-scale centered at the middle of the Ringvent bathymetric expression is provided and used in Figure 4. C. Northwest to southeast seismic profile (SO-118) with a projected location of the paired IODP X385 sites discussed in here. D. Detail seismic profile (AH-0102) of IODP X385 Sites U1545 and U1546. E. Detailed seismic (AH-2627) of IODP X385 Sites U1547 and U1548. Seismic profiles used in this study are presented in Supporting Information (SI-2). Lithostratigraphic column are based on IODP X385 (Teske

et a., 2021a). These units have been correlated to seismic horizons following Lizarralde et al. (2023) and the principles of core-log seismic integration, see insert C right panel.

2. Geological setting

The study area focuses on shallow sills with distinct geometries: the first one, drilled at Site U1546, is a flat sill well imaged by 2D seismic data with evidence of vertical pipes rooting at the sill and piercing the paleo-seafloor (Fig. 1D; Lizarralde et al., 2023; Cheviet et al., 2023). The second sill, drilled at Sites U1547 and U1548 (Fig. 1B), is inferred to be the root of a circular hydrothermal vent system organized along a narrow, ~10 meter high, ~600 m in diameter circular feature referred to as Ringvent. It is located in the northwestern part of the Guaymas Basin (Fig. 1, i.e. 20 km southeast to the massive sill at Site U1546). Ringvent is pocked by nine to ten pipe-like depressions at its crest. The spacing between vents ranges from 100 to 200 meters. The seafloor outside the ring of vents dips gently and radially outward, while the seafloor inside the Ringvent ridge forms a rather flat dome (Fig. 1B). During *Alvin* dives shimmering fluids were observed emerging from nearby mineral concretions covered with sulfur-oxidizing microbial mats, located on the ridge of Ringvent (Teske et al., 2019). The observed chemosynthetic ecosystems (i.e. microbial mats and symbiont-dependent invertebrates, i.e. tube worms) are supported by low-temperature hydrothermal system of 75°C (in-situ temperature probe measurements conducted during *Alvin* dives 4864 and 4865; Teske et al., 2019). This relatively low temperature venting suggests two possible origins of the hydrothermal fluids: (1) a mild epithermal fluid flow powered by a veining stage of a cooling of the magma plumbing system, or (2) a deep origin of the fluid guided passively to the seafloor via existing fluid pathways.

2.1. IODP Sites U1545 and U1546

Both IODP Sites U1545 and U1546 in the northwestern part of Guaymas Basin comprise seven holes, reaching a maximum depth of 500 m below the seafloor (mbsf) at both sites (mbsf; Teske et al., 2021b,c). These paired sites are only one kilometer apart (Fig. 1A,C,D). Drilling at Site U1545 (3 holes) recovered a continuous undisturbed stratigraphic sequence of the basin, down to 482 mbsf where a one-meter-thick sill was encountered. Drilling beyond 500 mbsf was deemed unsafe after headspace analyses of gas showed high concentrations of long-chain hydrocarbons with the methane/ethane (C1/C2) ratio dropping below 100 at a depth greater than 483 mbsf (Teske et al., 2021b). The overlying undisturbed sediment section is considered to be representative of the lithostratigraphic column of the northern part of the Guaymas Basin. The top 330 m of sediments have been divided into three subunits (1-A,B,C, Fig. 1C; further details in Persad and Marsaglia, 2023) that are characterized by silica-rich mud compositions with various proportions of siliceous biogenic (diatoms) and terrigenous particles (clay minerals and silt), containing millimeter-to-centimeter-sized carbonate nodules (Teske et al., 2021b). The fourth subunit (1-D), below 330 mbsf, is characterized by siliceous claystone and corresponds to a lithology where biosiliceous opal-A has diagenetically transformed into opal-CT (Figs. 1C, 2, and 3). This major diagenetic transition is accompanied by a steep downward increase in density and P-wave velocities that is caused by a decrease in porosity, diverging from the normal compaction curve of the wet unconsolidated sediments above (see SI-1, Fig. SI-1-1). The transition is also reflected in the rheology by an abrupt increase in shear strength marking the transition from an unconsolidated wet sediment to more lithified sedimentary rock (Fig. 2). The opal-A/CT transition is extensively documented based on IODP Sites U1545 and U1546 (Aiello et al., 2024; Cheviet et al., 2023; Lizarralde et al., 2023). A comparative summary of the petrophysical properties of host sediments for the studied sites is presented in Supporting Information SI-1.

In contrast to Site U1545, Site U1546 (4 holes) sediments are intruded by a 75-m-thick sill below 355.5 mbsf (Teske et al., 2021c). Except for this massive sill intrusion, the lithostratigraphic subunits 1-A, -B, and -C, are found at a depth similar to reference Site U1545 (Fig. 1C, 3A,B; further details in Persad and Marsaglia 2023). Notably, the opal-A/CT transition occurs at the same depth (Fig. 1C). The massive Site U1546 sill is made of aphanitic basalt at the margins transitioning to moderately altered medium-grained doleritic rock with a 25-m-thick more coarse-grained gabbroic texture just above the center of the sill. Despite these textural variations, the sill has a relatively homogeneous basaltic bulk rock composition (Teske et al., 2021c). The main minerals are plagioclase and clinopyroxenes with accessory alteration minerals such as clay, carbonate, and oxides minerals.

The sill at Site U1546 is well imaged by 2D seismic data (Fig. 1C). Its general geometry is flat and is roughly circular in map view with a diameter of 2.4 km (Lizarralde et al., 2023). Seismic images show narrow vertical channels found at a depth range from just above the sill (355.5 mbsf) to 130–160 m below the present-day seafloor (depth estimates are based on Lizarralde et al., 2023). These channels are interpreted as expressions of the hydrothermal fluid flow circulation associated with metamorphic contact aureole processes active during crystallization and cooling of the sill found at Site U1546 (Cheviet et al., 2023; Lizarralde et al., 2023). Consistent with previous studies of hydrothermal vent-related activity during sill emplacement (e.g., Jamtveit et al., 2004), the top of vertical pipes observed in the seismic data is interpreted as the vent mouths at the paleo-seafloor (Lizarralde et al., 2023). Using the re-evaluated average sedimentation rates in the Guaymas Basin of ~1 m/kyr (established by IODP X385; Teske et al., 2021a), it has been estimated that the sill at Site U1546 was emplaced between 185,000 and 95,000 years ago (see depth of the seismic reflector B3 and Y in supplementary material of Lizarralde et al., 2023). To illustrate this in the present-day context, we have located where the sill would be positioned in the present-day lithostratigraphic column of Site U1545 (Fig. 2, using an emplacement age of 100.5 ka). However, given the age estimate variations of the depth of the paleo-seafloor at the time of emplacement the top margin of the reconstructed sill emplacement depth can vary from 260.5 mbsf to 175.5 mbsf, and from 335.5 mbsf to 250.45 mbsf for the bottom margin (in a present-day lithostratigraphic column, Fig. 2A). This visually illustrates insights provided by Aiello et al., (2022) and conclusions of Cheviet et al. (2023), that the emplacement of the flat sill at Site U1546 was controlled by changes in the rheological properties of the sediments that are associated with the transition from opal-A to opal-CT.

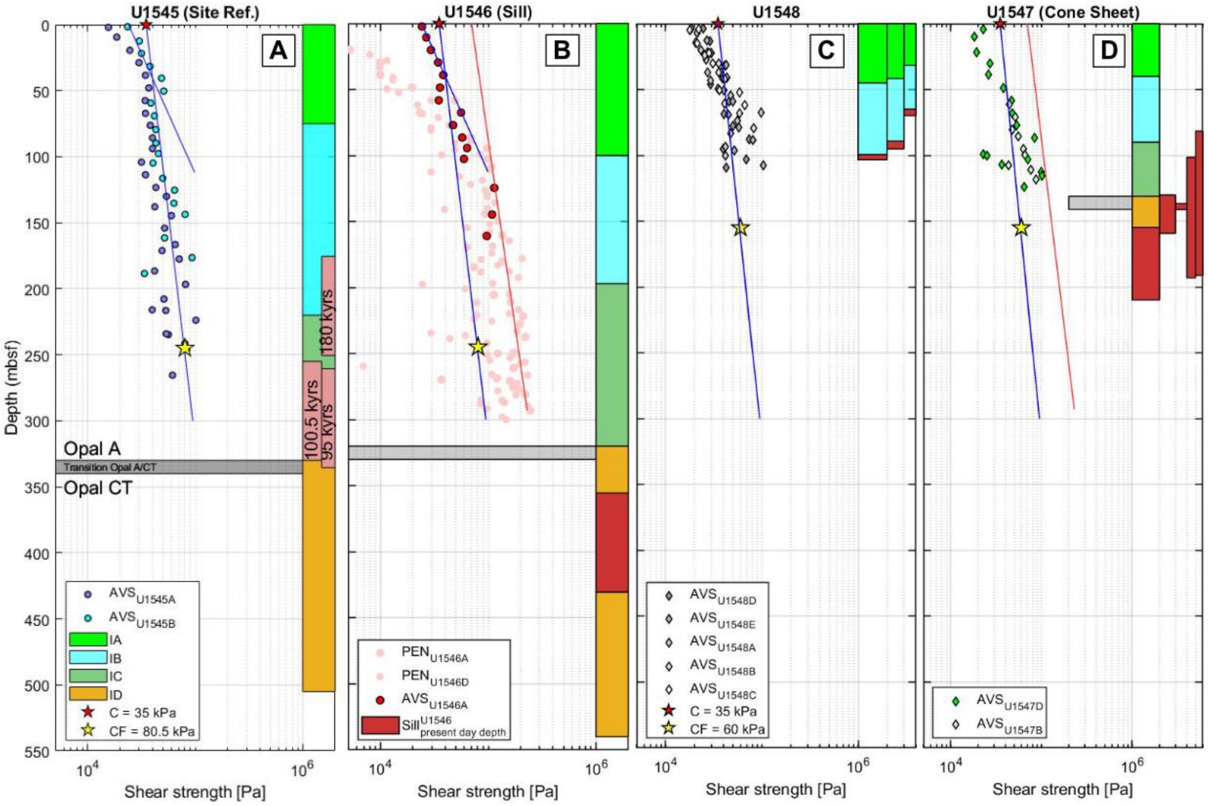

Figure 2. Shear strength measurements at the paired IODP X385 Sites U1545-U1546 and U1547-U1548. A. Site U1545 showing the rheological properties of the sediments unaffected by contact metamorphism process and thus the reference conditions prior to sill emplacement. The range of emplacement depths for the sill U1546 is calculated assuming the distinct overburden thicknesses estimated from the two potential maximum and minimum paleoseafloor reflectors detected in Lizarralde et al. (2023, i.e. 95 mbsf, and 180 mbsf, see Supporting Information SI-2, Fig. S2-2). B. Site U1546 show the rheological properties of the sediments at a site where sill intrusion occurred in the past, i.e. between 95 and 180 ka; Lizarralde et al., 2023). We observe that the depth reconstruction associated with the youngest age estimate (insert A) places the base of the reconstructed depth of the sill U1546 precisely on the opal-A/CT transition. C-D. Sediment rheological properties of the sediments at sites where sill emplacement occurred at a very shallow depth (top contact ranges between: 64.8 mbsf (Site U1548) and 154.6 mbsf (Site U1547)). The blue and red lines in all plots represent best linear fit to measured values at respectively the sediment reference Site U1545 and the other sill intruded Sites U1546, U1547 and U1548. Note that for the sill intruded sites, values compare well whether the sill was recently emplaced (Site U1547-U1548) or sometime in the past (Site U1547).

2.2. IODP Sites U1547 and U1548

IODP Site U1548 includes five drill holes that cored the sediments in the direct periphery of the Ringvent HVC. Holes U1548A/B/C are within 200 meters distance from the edge of the Ringvent HVC and Holes U1548D/E are at a distance of ~700 m away from the edge of the Ringvent HVC (i.e.

1000 m from the center of Ringvent HVC perimeter, Fig. 1). Sediments at Site U1548 are representative of the Guaymas Basin, mainly composed of silica-rich diatom ooze with a porosity range between 76% at ~ 100 mbsf and 92% at the seafloor (see SI-1, Fig. SI-1-1B). The sulfate-methane transition zone (SMTZ) is reported at a depth of 75 mbsf in the most distant holes (U1548D and U1548E). Hole U1548A to U1548C penetrated into a massive igneous body (sill) at depths of ~100 mbsf (U1548A), ~85 mbsf (U1548B), and ~65 mbsf (U1548C), respectivelly (Teske et al., 2021d). This interface between sediment and sill marks the lowest value in the porewater sulfate concentration profile, and is followed by a rise in methane concentration with increasing penetration into the sills (Teske et al., 2021d).

IODP Site U1547 includes five holes drilled within the perimeter of the Ringvent HVC (Fig. 1E). Figure 4B illustrates the depth of the sediment-sill interface (see Tab. SI-1-2) along a profile where IODP holes are projected with respect to the distance to the Ringvent HVC center. Porosity measurements show that the depth of the sill-sediment interface varies between ~80 and 155 mbsf (Teske et al., 2021d). The recovered igneous material shows a medium-grained texture punctuated by a high density of 0.5 cm large vesicles with various degrees of carbonate precipitation infill. Thin sections show a matrix of plagioclase and clinopyroxene (Teske et al., 2021d). Even the deepest holes did not reach the bottom of the igneous body. Shipboard bulk-rock analyses conducted by Inductively Coupled Plasma-Optical Emission Spectroscopy (ICP-OES) consistently yielded a basaltic composition (Teske et al., 2021d). Finally, structural evidence for columnar joints was found in the form of 120° angles between planar surfaces (Teske et al., 2021d).

The measured porosity of the sill at Site U1547 is particularly wide-ranging, from 10–20% (Teske et al., 2021d), whilst the sill drilled at Site U1546 shows low porosity values generally below 5% (Teske et al., 2021d). The latter are consistent with basaltic sill intrusions regardless of emplacement settings. This comparison applies to basalt of similarly fine- to medium-grained texture and excludes the coarse-grained gabbroic texture found at Site U1546 which yielded porosity values between 7.5 and 15%. Vesicles are generally absent from the reference sill intrusion at Site U1546 except for one sample near the top margin.

Sediments recovered at Sites U1547 and U1548 are characteristic of the Guaymas Basin, and consist of mostly biogenic silica-rich diatom ooze, although the siliciclastic component is more significant than at Sites U1545 and U1546. In the central Ringvent area, siliceous claystone has been identified in the deepest part of the most central Hole U1547B (Subunit ID). The main components are clays with opal-CT and pyrite framboids (Teske et al., 2021d). The silica phase transition from opal-A to opal-CT occurs in the sediments adjacent to the sill (Cheviet et al., 2023; Aiello et al., 2024), which suggests that they may have been considerably influenced by contact metamorphism.

3. Methods and Data

Seismic data used in this study are from R/V *Sonne* Leg SO241, and R/V *Alpha Helix* Leg AH1605. Information on seismic data acquisition can be found in the respective cruise reports (Berndt et al., 2015). A total of four seismic lines from two sets of 2D seismic are used in this study (Fig. 1). The R/V *Sonne* Leg SO241 data were collected by GEOMAR in 2015 (Berndt et al., 2015), and the R/V Alpha Helix Leg AH1605 data were collected by CICESE in 2016. Although all the lines have been considered during the analysis, we report here only two lines from the AH campaign AH-0102 and AH-2627 and one line from SO241 (Line 118, Fig. 1; see also Supporting Information SI-2). High-resolution bathymetry data for the Ringvent HVC was collected by the autonomous underwater vehicle (AUV) *Sentry* during the R/V *Atlantis* cruise AT36-06 in 2016 (Teske et al., 2019).

IODP petrophysical and basic lithostratigraphic data presented in this study are used first to constrain the transition between the overburden sediment and the main sill at Site U1547 (Teske et al., 2021d). The primary petrophysical proxies used are density, P-wave, and porosity data (see Teske et al. 2021e for acquisition methods and a summary of the data in Supporting Information-1A (SI-1A)).

Igneous (sill) samples analyzed in this study are from the reference sill of Site U1546 (six samples) and the sill found at Site U1547 (eight samples; Tab. SI-1-1). All 14 samples were examined petrographically (Fig. 3). All samples have a corresponding shipboard moisture and density (MAD) analysis provided by IODP X385 within 3.5 meters from the studied samples. A dedicated additional density and porosity measurement has been conducted on Section U1547B-35X-1 (Tab. SI-1-1) using the same instrument and method as on R/V *JOIDES Resolution* (see MAD measurements in the method chapter, Teske et al., 2021e).

Micro-CT measurements have been conducted on four samples from Hole U1546C and five samples from three different holes of IODP Site U1547. Micro-CT scans have been conducted using a ProCon CT-ALPHA system of the MAPEX Core Facility for Materials Analytics (DFG# 434618658), University of Bremen, Germany. Quarter round cores or fragments were scanned with a beam intensity of 125 kV, an energy flux of 300 μA, and a copper filter, using a 360° rotation. Reconstruction of the spatial information on the linear attenuation coefficient was done with the X-AID software (MITOS GmbH). Filtering of the raw data, volume reconstruction, segmentation, and volume/surface rendering were done using Avizo 2022.1 (ThermoFisher Scientific). A first-order scanning was conducted on 10 of the 14 samples available for this study (Fig. 3). A higher resolution measurement has been applied to Section U1547B-35X1 (using the ZEISS Xradia 520 Versa at 120 kV, 10W, Zeiss filter E6) to constrain in detail the effect of secondary pore space filling by carbonate.

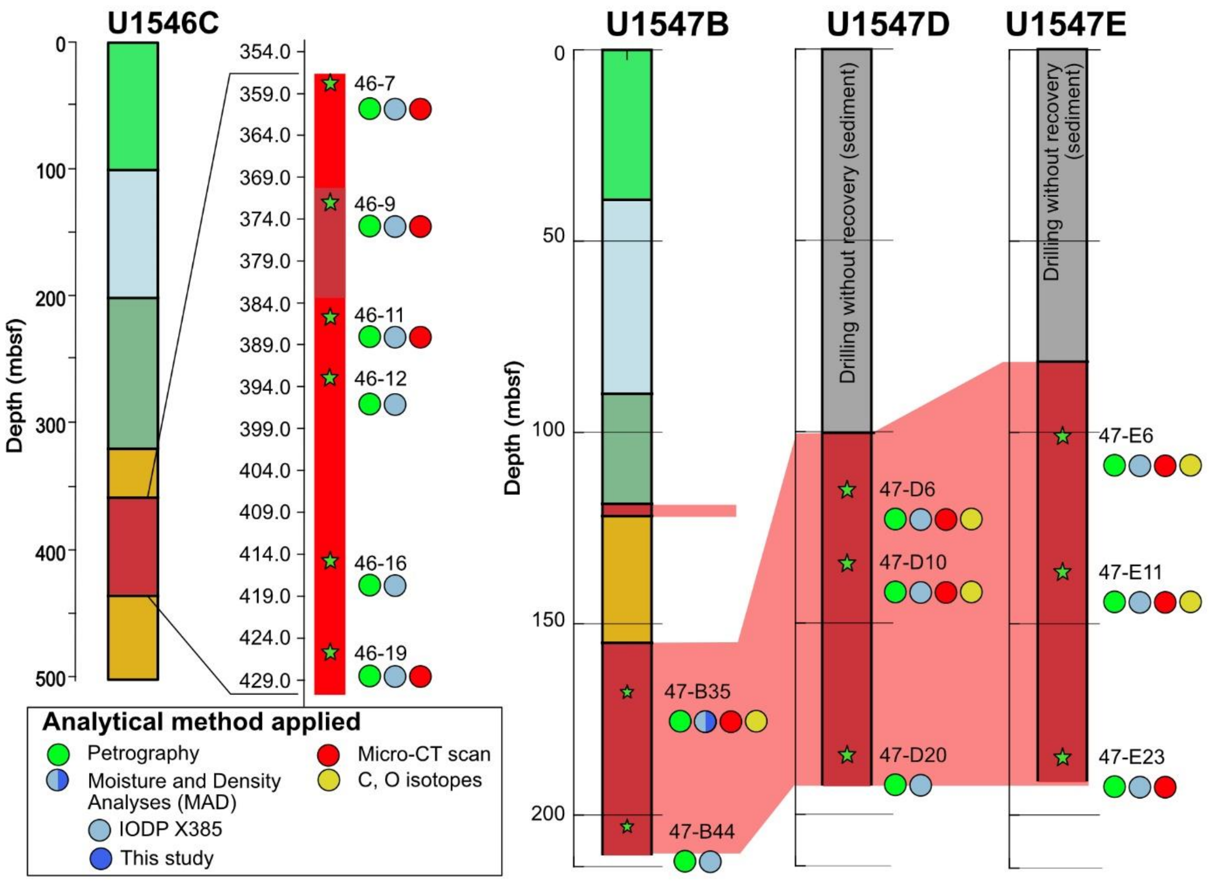

Figure 3. Samples analyzed in this study are located by stars on their corresponding stratigraphic columns (Sites U1546 and U1547). Refer to the legend for the analytical method applied to each sample. Simplified sample identifier can be related to the IODP ID in Tab. SI-1-1, along with each sample corresponding depths in respective holes, and distances from the top and bottom sill-sediment interfaces.

Here we provide here an in-depth analysis of the sill porosities comparing measurements from the two distinct sills found at Site U1547 and Site U1546, respectivelly. Two methods of measurements were used: MAD measurements quantified the void percentage in a given sample, and X-ray microtomography (micro-CT) scanning provided a 3D image rendering of the sample texture and mineral distribution as well as an evaluation of void space shapes, sizes and connectivity. MAD measurements reported in this study are part of the IODP X385 shipboard database (available from the LIMS online report (LORE) portal: https://web.iodp.tamu.edu/LORE/). Here we add two additional measurements on aliquots from sample U1547B-35X-1-16-22 (Fig. 3; Tab. SI-1-1) to address the greater ground mass heterogeneity associated with the large vesicles found in the sill at Site U1547. The same sample was measured by micro-CT scanning at two different resolutions in order to evaluate the detection limits of both methods.

Seven samples of calcium carbonate infill of large vesicles were collected by micro-drilling, then powdered and measured for carbon and oxygen isotopes (Fig. 3, Tab. SI-1-1). The samples are from three different holes (B, D, and E) of Site U1547. Measurements were conducted at MARUM, Center for Marine Environmental Sciences, University of Bremen, on a Finnigan MAT 252 gas isotope ratio mass spectrometer connected to a Kiel III automated carbonate preparation device operated at 75 °C. Data are reported in the usual delta-notation versus the Vienna Pee Dee Belemnite (VPDB) scale for d13C, and versus the Vienna Standard Mean Ocean Water (VSMOW) scale for d18O. The instrument was calibrated against the house standard (ground Solnhofen limestone), which in turn was calibrated against the National Bureau of Standards (NBS) 19 calcite (limestone). Over the measurement period the standard deviations of the house standard were 0.02‰ for $\delta^{13}C$ and 0.09‰ for $\delta^{18}O$.

4. Results

4.1 Geological reconstruction - a funnel-shaped sill at the Ringvent area

Our geological reconstruction builds upon the concept that the lateral extent of the Ringvent HVC circular morphological expression at the seafloor reflects a planar projection of an equally circular geometry of a sill at depth (Fig. 1). The IODP holes are projected onto a 2D cross-section (Fig. 4A, Tab. 1). Using drill holes from Site U1547 and U1548, we mapped the transition between the sediment and the top of a massive sill (Fig. 4B). The interface between the sediments and the top of the sill is located at ~80 to 150 mbsf (Tab. SI-1-2). Assuming that the slope of the sill-sediment interface does not vary, we estimate that the edge of the sill lies ~30 m below the ring of hydrothermal vents at the seafloor (Fig. 4A). The inward-dipping seafloor and the observed depth of the sill in the boreholes suggest that the Ringvent sill has a funnel-shaped geometry (Fig. 4D).

Table 1. IODP holes distance with respect to the sill center and the sill edges at Site U1547.

IODP Exp 385 Site	Latitude (°)	Longitude (°)	Seafloor Depth (m)	IODP Holes Exp. 385	Distance with respect to the sill centre (m)	Distance with respect to the sill edge (m)
U1547	27.5076	-111.6783	1733.7	U1547B	75.0	-225.0
	27.5069	-111.6789	1732.2	U1547C	78.1	-221.9
	27.5074	-111.6784	1732.2	U1547A	96.9	-203.1
	27.5066	-111.6791	1732.2	U1547D	103.1	-196.9
	27.5060	-111.6796	1732.1	U1547E	171.9	-128.1
U1548	27.5041	-111.6811	1737.0	U1548C	375.0	75.0
	27.5042	-111.6810	1738.9	U1548B	409.4	109.4
	27.5045	-111.6808	1739.9	U1548A	434.4	134.4
	27.5089	-111.6898	1729.9	U1548E	900.0	600.0
	27.5081	-111.6882	1729.3	U1548D	1062.5	762.5

Using this IODP X385-derived information (sediment sill interface, Tab. SI-1-2) in combination with the available 2D seismic profiles collected across the Ringvent Site (AH-2627, Figs. 1B,E; 4C), the high amplitude and chaotic signature of the seismic facies above the sill points to the heterogeneous sediment and magmatic rocks that fills the cup formed by the top of the funnel-shaped sills (Fig. 4C, D). Two seismic lines acquired at the same distance and orientation from the Ringvent sill highlight two complementary aspects of the system. Line SO-118 (Fig. 1C) features a flat sill or a series of flat sills starting at 2.55 s depth (TWT, value converted to depth using a constant P-wave value of 1,500 m/s, ~150 mbsf). Cross-lines passing through the Ringvent site (AH-2627 and AH-2122) suggest that this flat sill or series of sills may extend continuously underneath and around the Ringvent structure. We interpret the reflection at ~2.4 s (TWT, i.e. ~50 mbsf) as an-out-of-plane reflection representing the top edge of the Ringvent funnel-shaped sill intrusion.

The overall thickness of the sill cannot be constrained because the seismic data do not show a clear base reflection, and of the five holes that pierced the sill at Site U1547 none penetrated it fully. However, a significantly different igneous lithology has been identified at the bottom of Hole U1547E, which shows an increased abundance of spherical cavities filled with clay minerals. Calcite-filled vesicles are almost entirely missing in this unit. This difference in lithology is associated with a change in magnetic susceptibility. Although other petrophysical parameters, such as density and porosity, remain relatively constant downhole, the pronounced difference in composition suggest that the bottom section of Hole U1547E probably represents the near-base of the Ringvent sill. Holes U1548A/B/C show a progressive shoaling of the sill-sediment interface towards the edge of the Ringvent HVC and point towards the same location underneath the Ringvent HVC as we extrapolate the sill-sediment interface outward from the center of Ringvent (Fig. 4C,D). The summary of the Ringvent sill inferred geometrical characteristics can be found in Supporting Information (SI-4).

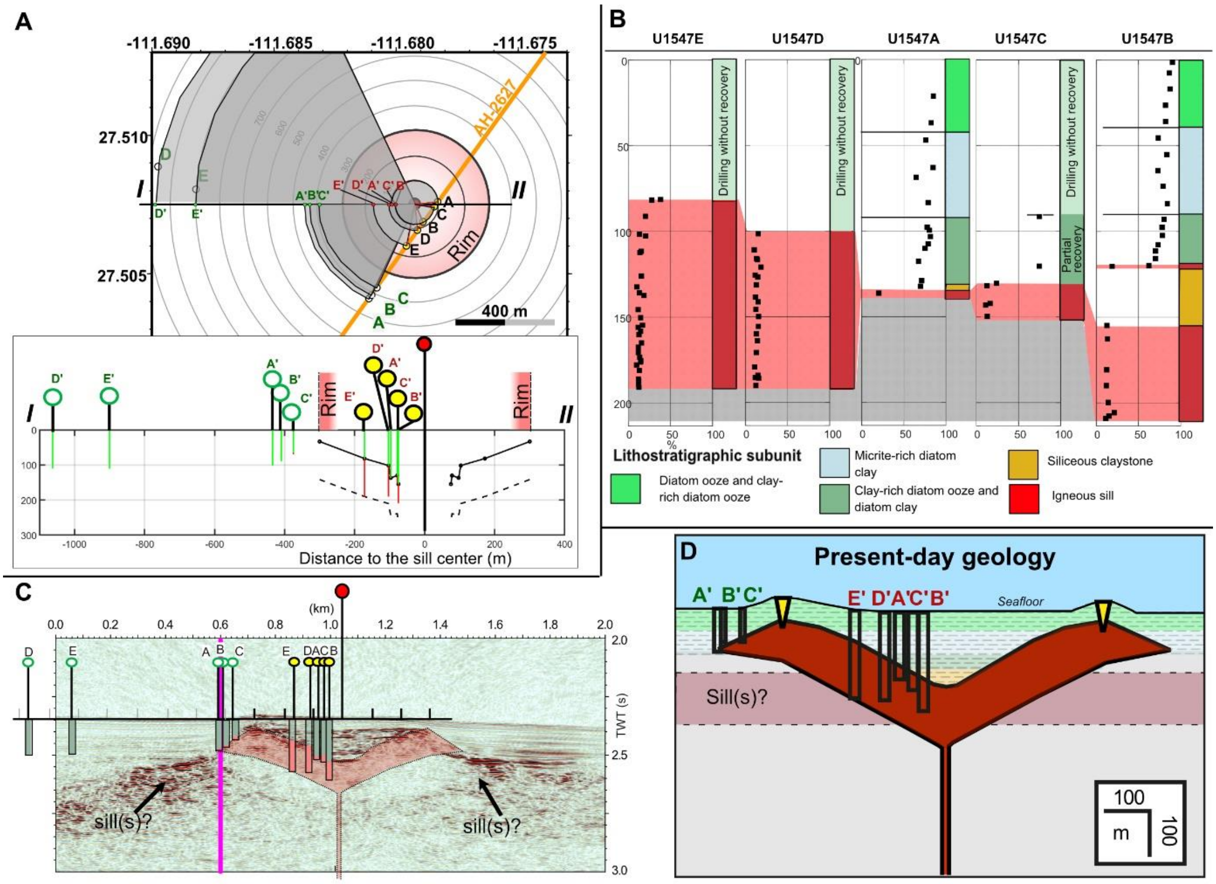

Figure 4. A-C. Correlation between seismic imaging and IODP drilling with indication of the sediment – igneous body interface. D. Interpretation of the present-day geology of the Ringvent system, i.e. subseafloor funnel-shaped sill and seafloor ring of hydrothermal vents.

4.2. Thermal state and source of the present-day hydrothermal fluids

To understand how the hydrothermal vent system is related to the funnel-shaped sill intrusion, we first establish the present-day thermal structure associated with both the deep and the shallow part of what we will further refer to as the Ringvent system. Here we use in-situ temperature measurements conducted while drilling at Sites U1547 and U1548 during IODP X385 (Teske et al., 2021d, Sarkar et al., 2022; Neumann et al., 2023). Aligned on our geological cross-section (Fig. 4A), we show the evolution of the geothermal gradients inferred from the most distal holes (U1548D/E) to increasingly closer holes to the edge of the Ringvent system, i.e., U1548A, U1548B, and U1548C, respectively (see SI-5, Fig. SI-5-3). The results indicate a consistent increase of the geothermal gradient and seafloor heat flow density from a background value of ~303°C/km (i.e., ~244 mW/m^2) in the most distant holes (U1548D/E) to a very high value of 1187°C/km in Hole U1548C (i.e., 929 mW/m^2), within 100 meters distance from the edge of the Ringvent system. An increase of 0.052 mW/m^2 of heat flow per one meter of lateral distance along our geological cross-section is observed between Holes U1548D/E and Hole U1548C. This is followed by an increase of 6.75 mW/m^2 per meter distance between Holes U1548C and U1548A at the direct periphery of the Ringvent system. This rapid increase suggests that the edge of the Ringvent system represents a local heat source.

Using our geological cross-section, we can infer that the geometry of the heat source anomaly coincides with the Ringvent ridge. However, the geothermal gradients and heat flow densities measured inside the perimeter of the bathymetric high formed by the ring of hydrothermal vents yield rather low values comparable to those found on the outer-edge of the Ringvent bathymetric high (i.e., geothermal gradient | heat flow for Hole U1547A: 500°C/km | 528mW/m^2; and for Hole U1547B: 656°C/km | 570 mW/m^2). These values are still higher than those of the most distant holes considered as reference (U1548D,E), suggesting that the thermal anomaly marking the Ringvent ridge is likely to be attributed to the up-flow of hot fluids.

To reconstruct the hydrothermal state of the system at depth, the following approach is applied. Wherever direct measurements at any given depth were made in an IODP hole, the temperature applies to our depth reconstruction. At a depth greater than any given hole was drilled, two reconstruction paths are weighted. The first path extrapolates the projected temperature from the geothermal gradient in the hole of interest. This option is valid for all holes, except those at the outer edge of the Ringvent system, which are under the influence of the local thermal anomaly. At a depth below 100 mbsf where the lower contact of the sill deepens towards the center of the Ringvent system, the distance between the holes and the sill edge increases (Fig. SI-5-3 projected holes A', B', C'). Thus, the second path is that at a depth >100 mbsf, we assume that the background geothermal gradient prevails for Holes U1548A/B/C at depths greater than 150 mbsf (vertical blue dashed lines extrapolating U1548A',B',C' at depth Fig. SI-5-3).

The temperatures obtained from each hole at the seafloor, 50, 100, 150, and 300 mbsf, respectively, are reported in Table 2. The values indicate that the temperature anomaly progressively decreases at depth greater than 100 mbsf in the three holes located in the direct vicinity of the Ringvent system. This interpretation of the temperature profile is consistent with the reconstructed Ringvent sill geometry and suggests that fluid flow at a comparatively moderate temperature (~75−80°C) fluid flow pathway is controlled by the depth at which the lower edge of the Ringvent sill resides. This model indicates that the source of the hydrothermal fluids is at ~300 mbsf, i.e. the reconstructed depth of the base of the funnel-shaped sill intrusion. Additionally, the geothermal profile inside the Ringvent ridge appears to be controlled by an upper value at the sill sediment interface that is 85°C. This suggests that the hydrothermal fluids are deeply sourced from the depth of the basin and can percolate inside the funnel-shaped sill at Site U1547.

Table 2. Temperature value used to construct the thermal structure of the Ringvent system. IODP holes are displayed from the most distant hole to the closest hole from the Ringvent sill center (left to right). Values reported in the *IntV* column refer to interpolated values based on linear fit to the measured geothermal gradient (detailed in SI-5, Table SI-5-1). Values reported in the *Int* column refer to interpreted values corresponding to

either to the depth extrapolation (U1547A,B) or background values. Original values can be found in Teske et al. (2021b) and Neumann et al. (2023). T_0* is the surface temperature resulting from the analysis published by Neumann et al. (2023). Note that we take a median value in case where two holes are reported together. Site U1548 holes reside outside Ringvent HVC while the Site U1547 holes are located inside this HVC.

Site	U1548		U1548		U1548		U1548		U1547	
Hole	D	E	A		B		C		A	B
Distance from Ringvent center (m)	1066	900	434		409		375		97	75
Meters below seafloor (mbsf)	*IntV*	*Int*	*IntV*	*Int*	*IntV*	*Int*	*IntV*	*Int*	*IntV*	*Int*
0 (T_0*)	4.5	-	21.9	-	19.0	-	16.1	-	16.8	-
50	17.1	-	45.3	-	49.9	-	62.7	-	39.5	-
100	29.8	-	68.8	-	80.8	-	109.4	-	62.2	-
150	42.4	-	92.2	42.4	111.8	42.4	156.1	42.4	85.0	85.0
300	80.2	-	162.5	80.2	204.6	80.2	269.1	80.2	/	/

4.3. Petrographic summary

The sill at Site U1546 has a relatively broad textural variation from fine- to coarse-grained. Samples with a fined-grained matrix (made of dominantly plagioclase microlites and some clinopyroxene) are remarkable because they are interspersed with large, centimeter-sized plagioclase phenocrysts, which often have sieve texture; they are particularly prominently near the sill margin (samples 46-7, 46-16, 46-19, Tab. SI-1-1; Fig. SI-6-1). The large plagioclase phenocrysts have a highly irregular grain boundary, indicating reaction with the surrounding melt. In contrast, the abundant plagioclase phenocrysts in the coarser-grained central part of the sill show almost no sign of destabilized textures, and are instead intergrown with large clinopyroxenes crystals (samples 46-12, 46-9, Tab. SI-1-1; Fig. SI-6-1). The same central part of the sill also shows abundant amphiboles (including arfvedsonite), aenigmatites, micas, olivines, altered pyroxenes (aegirine) and secondary clay minerals samples (46-12, 46-11, 46-9; Tab. SI-1-1; Fig. SI-6-1). These mineral assemblages are highly common for oceanic basalts and suggest significant metasomatic mass transfer that is likely induced by large amounts of sediment-derived fluids that infiltrated the sill at Site U1546.

Although the Ringvent sill resembles the Site U1546 sill in terms of primary mineral composition, the two sills are very different in terms of texture and porosity. Firstly, the Ringvent sill is comparatively uniform in texture. It is more fined-grained throughout and shows a high abundance of mostly large circular vesicles that are up to 3 mm in diameter. Petrographic analysis shows that the vesicles are often surrounded by areas that are darker in appearance and often feature elongated clinopyroxene with comb texture (e.g., samples 47-B35, 47-E6, Tab. SI-1-1; Fig. SI-5-2A-B, G-N). Fe-Ti oxides have been detected in abundance in these darker areas as well as coatings at the outer rim of the vesicles. Calcium carbonate, as well as sometimes smectite and sulphides (pyrites) fill the pore space partially or completely. This general petrography only changes only in Hole U1547E below ~175 mbsf where secondary clay minerals appear in higher abundance (sample 47-E23, Tab. SI-1-1; Fig. SI-5-2E,F).

4.4 Textural analysis (Micro-CT)

Porosity is one of the petrophysical parameters that displays the most striking difference between the flat sill at Site U1546 and the funnel-shaped sill at Site U1547 (Fig. 7; see also Figure SI-1-2). It is up to 15% higher in the funnel-shaped intrusion compared to the flat sill which shows relatively standard porosity for sills (2.5–4.2%). Here we have analyzed a total of ten samples from both sills, using the micro-CT technique, to assess if the relatively abundant vesicles at Site U1547 could explain the porosity increase compared to Site U1546 where vesicles are generally absent.

Quantitative digital image analysis (QDIA) of micro-CT-derived volume reconstructions is dependent on the resolution of the scans (i.e., voxel size - VS). Any pore diameter falling below the VS resolution is not accounted for. Figure 5 compares the porosity values measured by MAD procedure and micro-CT (see legend in Fig. 5A). Based on shipboard measurements, the sill at Site U1546 had shown a relatively low porosity (i.e., 2.5–4.2% by MAD). Corresponding QDIA of these samples, however, are close to zero (0.03–1.10%, see Tab. 3). Pores smaller than twice the VS (8–16 µm) remain below detection limit. This means that a large fraction of void sizes in samples 46-7, 46-11 and 46-19 are likely below 20 to 30 µm in diameter. In order to account for the MAD measurements with porosity values up to 3.43–3.46 %, we have applied a porosity correction to the micro-CT measurements by adding a value of 3.40% to all micro-CT-based QDIA for the Site U1546 sill (Fig. 5A). This processing step places all micro-CT-based QDIA in the range of the values obtained by the MAD measurement method (see yellow star symbols falling into pale gray field, Fig. 5A). We have applied the same principle to measurements conducted on samples from Site U1547 (Fig. 5B,C,D). At Site U1547, a larger difference is observed between the results of the micro-CT and MAD measurements (i.e., 8.48%), pointing to a different pore size distribution below the micro-CT detection limit. Adding this value to all micro-CT measurements of the Ringvent sill (Site U1547) provides “corrected” porosity values that are in the range of MAD measurements (Fig. 5B,C,D).

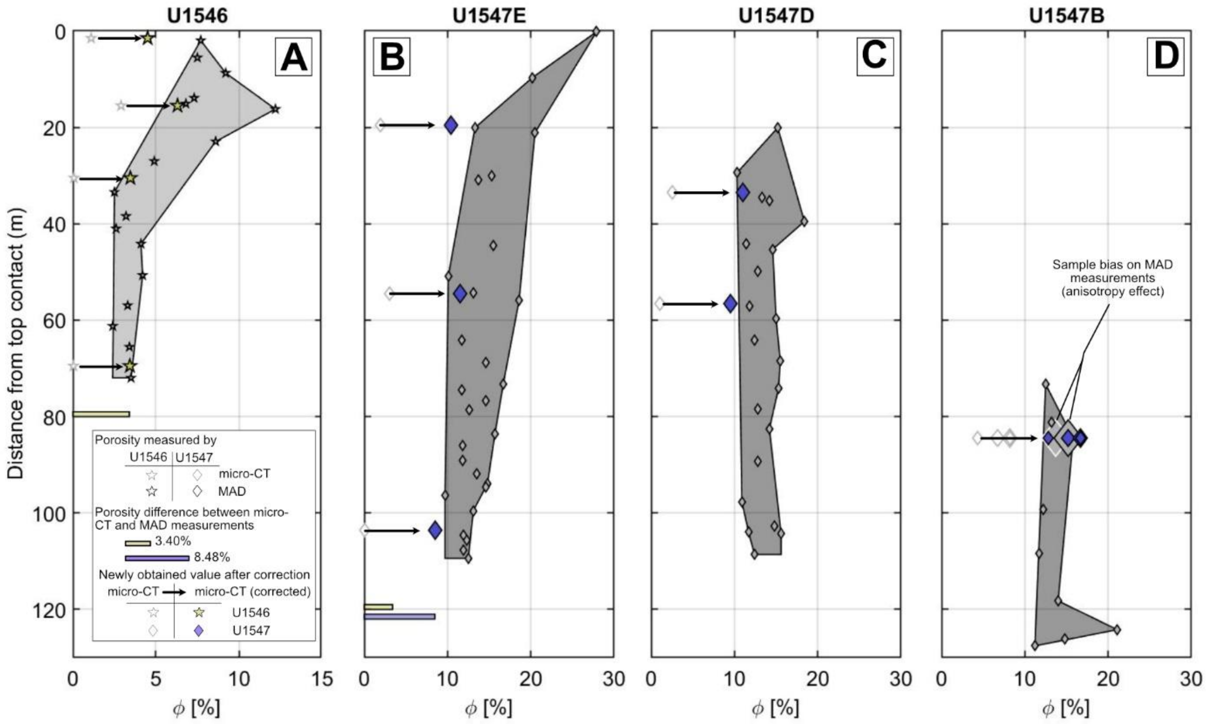

Figure 5. Comparison of moisture and density measurements (MAD) and micro-CT-based digital image analysis of porosity. Shaded fields depict the range of MAD data. In comparison, micro-CT-derived porosities (stars and diamonds) remain much lower. This difference reveals that a large fraction of the porosity detected by MAD is hosted in void diameters below the resolution of the X-ray tomography scans.

Microscopic observations and micro-CT imaging of the large vesicles indicate that they may still be empty, partially or entirely filled by carbonate and clay minerals depending on the sample locations. To estimate the initial porosity, we focus on two samples that show: 1) a relatively common example of large vesicles partially filled with calcite (sample 47-B35, Tab. SI-1-1, Figs. 3, 6), and 2) a singular sample from one of the deepest parts of the drilled sill at Site U1547 that has abundant clay minerals filling the pore space (sample 47-E23, Tab. SI-1-1, Figs. 3, SI-7-1). Using an image processing tool to digitally remove secondary calcite mineralization in selected large vesicles, we estimate that restoring the initial porosity (Fig. 6) in sample U1547B-35X-1-16-22 (Tab. SI-1-1) could account for a porosity increase of 3.9% depending on resolution (i.e., VS; Fig. 5C, Tab. 3).

This digitally inferred porosity increase is confirmed by a second sample (47-E23, Tab. SI-1-1, Figs. 3, SI-7-1), processed by digital removal of clay minerals filling the pore space found at the largest distance from the top contact (i.e., bottom of Hole U1547E). Here, the sample porosity measured by the two distinct methods initially showed a porosity of 0.06% (micro-CT) and 11.9% (MAD). The digital evaluation of the space occupied by the clay mineral in the sample revealed that the initial porosity may be as high as 23.30% (Fig. SI-7-1, Tab. 3). The fact that this lowermost part of the sill is mostly filled with clay minerals suggests a more pronounced and persistent low-temperature hydrothermal circulation. Thus, some clay mineralization may be attributed to alteration of the magmatic phases. Consequently, 23% of initial porosity may be regarded as an overestimation. In cases where clay minerals are more abundant, systematically higher porosity values obtained by micro-CT are potentially a contribution from both imaging resolution (VS) and desiccated clay minerals. Specifically, the MAD measurement saturation procedure is followed by a drying process at 105°C ± 5°C (Teske et al., 2021e) that is likely to desiccate the re-hydrated clay minerals. This results in an excessive volume loss of the clay, opening the pore space to void detected as open porosity during the MAD measurement.

Finally, we have also conducted additional MAD measurements on the sample U1547B-35X-1-16-22 (Tab. SI-1-1) to evaluate what could be the effect of the sample anisotropy visible in Figure 6 on the MAD measurements. For this purpose we cut the sample in two and measured the two aliquots separately at the MARUM Geotechnical Laboratory using the same MAD instrument and procedure as in the R/V *JOIDES Resolution* petrophysical laboratory. The results indicate a difference of 1.44% between the two obtained values, i.e. 13.74 and 15.18% (large diamond symbols Fig. 5C). This value may thus be considered as a good error bar for all MAD measurements. Overall, we conclude here that the porosity of the Ringvent sill ranges between ~10 and 20%.

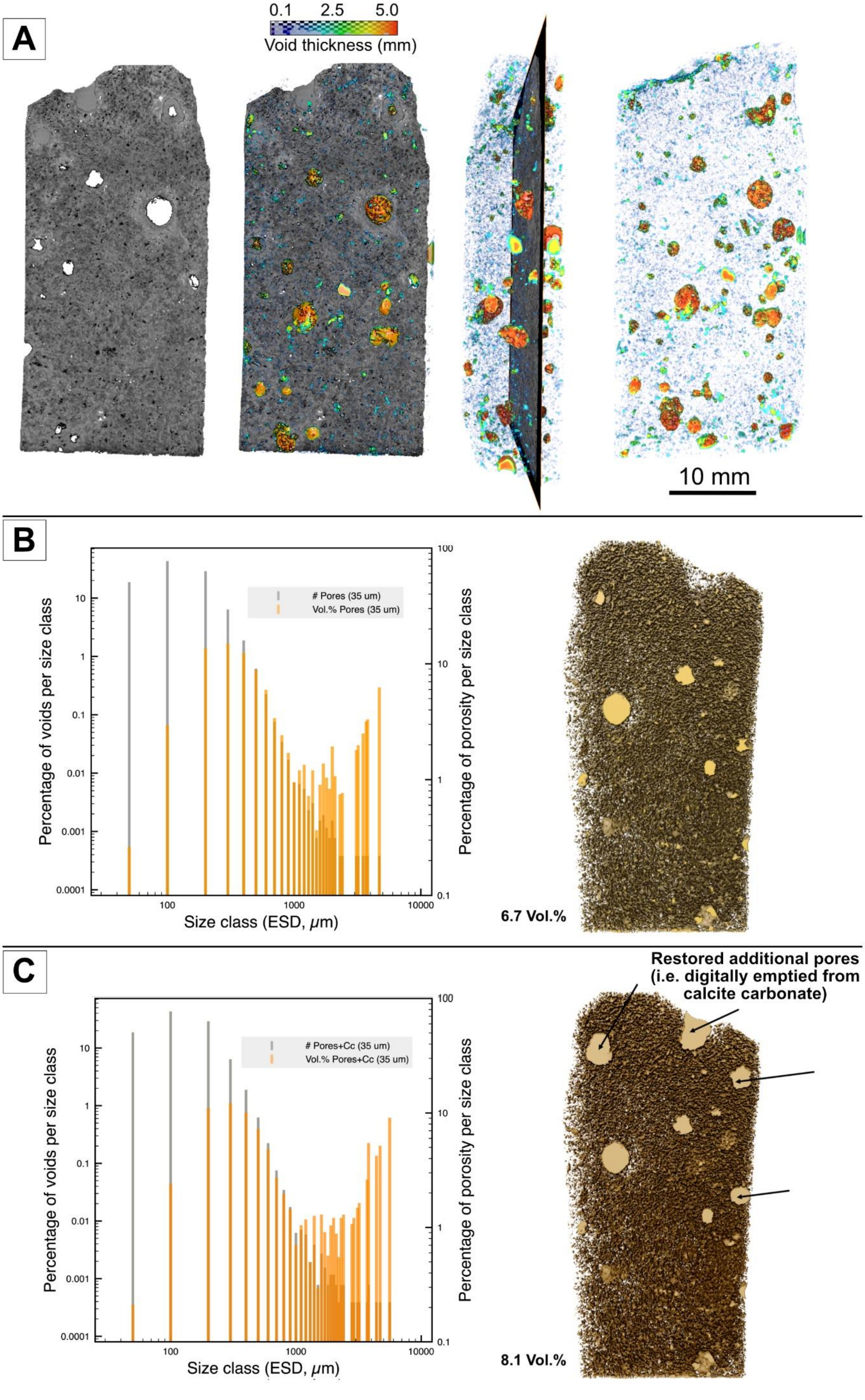
A
0.1 2.5 5.0
Void thickness (mm)
10 mm
B
Percentage of voids per size class
Percentage of porosity per size class
Size class (ESD, μm)
Pores (35 um)
Vol.% Pores (35 um)
0.0001
0.001
0.01
0.1
1
10
100
1000
10000
0.1
1
10
100
6.7 Vol.%
C
Percentage of voids per size class
Percentage of porosity per size class
Size class (ESD, μm)
Pores+Cc (35 um)
Vol.% Pores+Cc (35 um)
8.1 Vol.%
Restored additional pores
(i.e. digitally emptied from
calcite carbonate)

Figure 6. Illustration of the quantitative digital 3D image analysis of the micro-CT scan of Sample U1547B-35X-1-16-22 (Tab. SI-1-1, Fig. 3; 35,42 µm/voxel). A. Reconstructed image slice combined with the visualization of voids (color-coded with void thickness). B. Percentage of voids per size class in Equivalent spere diameter ESD. A few large voids account for the majority of porosity detectable within the voxel size-determined resolution. C. Porosity analysis applied after digitally removing secondary calcite mineralization. As can be seen in the associated volume rendering and in Table 3, the removal of calcite in four large pores increases porosity to about 8.20%.

Table 3. Summary of selected properties of the micro-CT-derived 3D image volumes. *The effect of digital removal of mineralization is visualized in Figs. 6 and SI-7-1.

Sample (simplified ID, Tab. SI-1-1)	Voxel size (µm)	Porosity % (voids)	Porosity % (voids + digitally remove mineralization)
46-7	9.97	1.10	n. a.
46-9	16.1	2.90	n. a.
46-11	8.05	0.06	n. a.
46-19	9.66	0.03	n. a.
47-B35	35.42	6.70	8.10 (Cc)*
47-B35 (hi-res)	8.82	4.30	8.20 (Cc)
47-D6	35.42	1.00	n. a.
47-D10	35.42	2.50	n. a.
47-E6	9.66	1.90	n. a.
47-E11	9.66	3.00	n. a.
47-E23	9.66	0.06	23.30 (clay)*

4.4. Isotopic composition of carbonate infill in the Ringvent sill

Calcium carbonate (calcite) found in vesicles and veins from the Ringvent sill show δ^{18}O (standard mean ocean water, SMOW) values range from 20.93 to 23.25‰ (Tab. 4, Fig. 10A; all δ^{18}O values reported hereafter refer to the SMOW standard). These values are considerably lower than values obtained from carbonate nodules hosted in subsurface sediments (33.7–35.3‰, data from Teske et al., 2019), and bulk sediment (29.80–31.59‰, data from Teske et al., 2019) found at the seafloor with near seawater composition. δ^{13}C (VPDB) values of the same carbonate analyzed here show variations between -8.22 and -2.20‰ (Tab. 4, Fig. 10A; all δ^{13}C values reported hereafter are in VPDB scale). These values are well in range with bulk sediment values found at the seafloor of the Ringvent system (29.9–32.6‰, Fig. 7A; Teske et al., 2019), whereas carbonate nodules present values that are generally much lower, ranging between -47 and -30‰ (Fig. 7A; Teske et al., 2019).

Table 4. Isotopic data of carbonate precipitation found in the Ringvent sill. Value reported are in VPDB scale for δ^{13}C and in SMOW scale for δ^{18}O. δ^{18}O values of the hydrothermal fluid used for the oxygen isotope

thermometry model is fixed at 2.5‰. ΔT represent the temperature difference between the calculated precipitation temperature of the calcites and the temperature at this depth considering the background geothermal gradient for the Ringvent system of Hole U1548DE (~303°C/km). Abbreviation: Hydrothermal Fluid (HF), composition (com.). Data are ordered by holes, each with increasing depth. Holes are ordered with respect to their relative position to Ringvent sill center (cf. Tab. 1, Fig. 4).

Sample (simplified ID, Tab. SI-1-1)	Depth (mbsf)	Actual T°C	$\delta^{13}C$ [‰]	$\delta^{18}O$ [‰]	HF comp. $\delta^{18}O$ [‰] SMOW	T°C calculated	ΔT
			(±1 s.d.) VPDB	(±1 s.d.) SMOW			$(T_{calculated}-T_{actual})$
47-B35	166	108.896	-4.3	21.95	2.5	81.5	35.1
47-B44	203	133.168	-8.22	23.85	2.5	67.5	11.7
47-D6	115	57.5	-2.2	23.25	2.5	71.7	56.2
47-D6 vein	115	57.5	-2.59	20.93	2.5	89.8	46.8
47-D10	135	67.5	-3.47	22.09	2.5	80.4	32.9
47-D20	184	92	-	-	2.5	-	-
47-E6	101	50.5	-3.96	22.86	2.5	74.6	44.6
47-E11	136	68	-7.05	21.99	2.5	81.2	42.3

We calculate the temperature of calcite formation assuming that oxygen isotope equilibrium existed between the calcite and the hydrothermal fluids with $\delta^{18}O$ values close to seawater due to interactions with basin sediments (Tab. 4). We use the oxygen isotope fractionation factor (see equation 5 in Peter and Shanks, 1992) for the calcite-water system after O’Neil et al. (1969) and Friedmann and O’Neil (1977). The calculated temperatures range from ~67 to ~90°C (Tab. 4). These results indicate calcite precipitation temperatures above the current geothermal gradient (500-656°C/km for location U1547AB, Tab. 4) for samples collected at depth above ~135 mbsf. While deeper samples yield a lower temperature compared to the current geothermal gradient at Site U1547. In Table 4 shows the calculated temperature difference between calcite precipitation temperatures and the background geothermal gradient (i.e., Holes U1548D and E: ~303°C/km, see Fig. SI-5-4). The simplest explanation for these temperature differences is that the Ringvent sill is acting as a conduit to drain deeper fluids. Using the geothermal gradient of the sediments in Holes U1548D/E (~303°C/km) we can show that hot fluids sourced at ~260-338 mbsf are consistent with precipitation temperatures of the calcites crystals sampled (see Fig. SI-5-4).

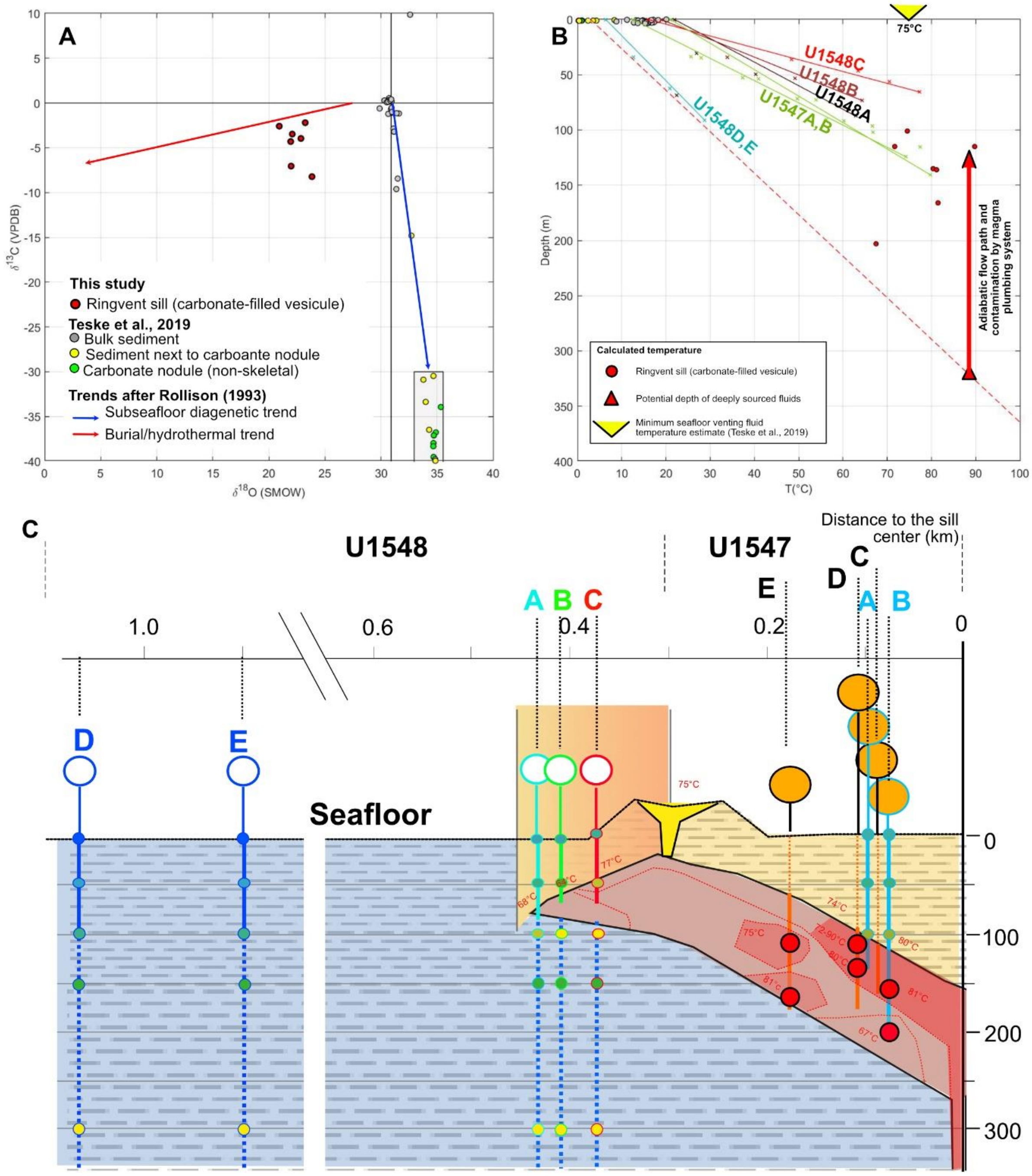

Figure 7. A. Cross plot of $\delta^{13}C$ versus $\delta^{18}O$ isotopic compositions of calcite. Other analyses are from subseafloor mini-cores from Teske et al. (2019), and represent bulk sediment and carbonate nodules. B. Result of the oxygen thermometer model (Tab. 4) displayed along depth together with the ambient geothermal gradients of Sites U1547-U1548. C. Positioning of the studied samples in the present-day thermal structure of the Ringvent system (see section 4.2). Symbols and color code for the sample can be found in legend of insert A and B. Inferred temperatures of calcite precipitation are reported in red.

5. Discussion

5.1. Implication for magma emplacement

Results of IODP X385 in the Guaymas Basin show that the mechanics of emplacement of shallow sills differs from sill emplacement at greater depth. This is due to the host shallow sediments that are unconsolidated and highly porous. These uppermost water-rich strata offer a minimal cohesive strength of the remaining overburden (Fig. 2) that prevents an elastic plate bending type of deformation. This has profound consequences for the space accommodation during sill emplacement. A good example of this is the sill found at Site U1546 that intruded just above the first diagenetic barrier at the opal-A/CT transition (Cheviet et al., 2023; Aiello et al., 2024). This sill is 75 m thick (*th*) at a width (*w*) of ~2.4 km (Tab. 5), yielding a thickness to width ratio in the order of 1×10^{-2}, a value one order of magnitude greater than the sills of the Jurassic saucer-shaped sills of the Golden Valley Sill Complex (GVSC) in South Africa (e.g., Galerne et al., 2008; Galerne et al., 2010). This means the sill emplaced at Site U1546 is relatively thick compared to its short lateral extent. Compaction of the overburden sediment up to the paleoseafloor has been demonstrated by seismic imaging (Lizarralde et al., 2023), and a doming of the paleoseafloor can be seen in seismic profiles (Fig. 1D).

The situation is different at the Ringvent system. Our combined analysis of the 2D seismic and IODP data from Site U1547 shows that the geometry of the sill associated with the Ringvent system is funnel-shaped, often referred to as cone sheet geometry in literature (e.g., Bailey et al., 1924; Philipps, 1974 Galland et al., 2014). The shallower emplacement of only 90 m compared to the sill at Site U1546 (emplacement depth at the time of emplacement, top margin: ~250 mbsf, cf. Fig. 2), dictates a switch between magma emplacement geometry from a flat sill to a funnel-shaped sill.

Funnel-shaped sill intrusions and saucer-shaped sill intrusions have been shown to form when the magma feeder source (i.e., a magma reservoir or a horizontal flat sill) interacts with the deformable overburden and the basin's free surface (e.g., Galland et al., 2009; Galerne et al., 2011; Galland and Scheibert 2013; Galland et al., 2014). Using laboratory-scaled experiments, Galland et al (2014) showed that dikes and funnel-shaped sills (or cone sheets) correspond to two distinct mechanical regimes separated by a sharp power law boundary. Results of Galland et al (2014) show that formation of dikes, sills, saucer-shaped sills, and funnel-shaped sills is governed by two dimensionless ratios. The first ratio $\Pi_1 = h/d$ describes the geometry of the magma source where h is the depth of emplacement and d is the intrusion width. The second ratio $\Pi_2 = \sigma_v/C$ compares the viscous stresses ($\sigma_v = \eta V/d$) induced by the flow of magma in a conduit of thickness d assuming a Poiseuille flow to the host rock strength defined by cohesion (C). Fields of characteristic parameter ranges, corresponding to different types of magma intrusion shape and reservoir are represented in Figure 8. This graph examines where the funnel-shaped sill from the Ringvent system plots compared to its deeper counterpart, that intruded as a flat sill only 90 meters deeper into the same soft, unconsolidated, and water-saturated sediment (diatom ooze).

Cohesion of the host sediment prior to emplacement can be inferred at Sites U1545 and U1548 (Fig. 2). To obtain this value, we consider the shear strength value of the sediment at the top contact with the sills, referred to as cohesive force (*CF*, Hajime, 1967) in soil mechanics. The value found for the sill at Site U1546, at the time of emplacement, is inferred to be 80.5 kPa and only 60 kPa for the shallower funnel-shaped intrusion emplaced at Site U1547 (yellow star in Fig. 2). This corresponds to a *CF* increment of ~230 Pa per meter of sediment. While the parameter Π_1 is kept constant for both sills, we assume a range of values for the parameter Π_2 (see Tab. 5, corresponding to the cyan- and magenta-filled symbols in Fig. 8). The latter parameter range has been obtained using the highest velocity values and, correspondingly, lowest viscosity values provided in literature (Galland et al., 2014 and references therein). The results indicate that the Site U1546 sill plots at the upper limit of the "Sills" field along Π_2, while the funnel shaped sill at Site U1547 plots close to the "Funnel-Shaped Sills" field of Galland et al. (2014).

These results validate and extend the *funnel-shaped sills* field in the diagram originally provided by Galland et al. (2014). They show that the range of natural parameters contributing to Π_1 yield much lower values than previously established for the "Funnel-Shaped Sill" field ($\Pi_1 = 0.26$ in this study versus $\Pi_1 = 3$ in Galland et al., 2014) and confirm the upper limit of the "Sills" field along the parameter Π_2 to have a lower limit value of $1x10^{-4}$. In terms of physical meaning, we interpret this result as a confirmation that the overburden sediment lithology in the context of the studied sills (Sites U1546 and U1547) has little to no elastic behavior in response to sill emplacement. This explains why the sill found at Site U1546 has a relatively high value of thickness over lateral extent. Using a linear range of variation of parameters between Sites U1546 and U1547 for cohesion and depth it can be shown that the depth of transition between flat and funnel-shaped sill intrusions is crossed at ~165 mbsf. This value is only ~10 m below the estimated depth of the top contact of the funnel-shaped sill at its deepest point (e.g. Fig. 4 and Fig. SI-5-3).

The parameter range used to calculate Π_2 is justified by the fact that the magma emplacement in both cases (the U1546 flat sill and the U1547-U1548 funnel-shaped sill) occurs in conditions where magma-sediment mingling dominates. Additionally, the evolution of the sill geometry towards a funnel-shaped morphology with decreasing intrusion depth is also consistent with numerous mechanistic studies (e.g., Galland et al., 2014; Haug et al., 2018). However, our findings suggest that the magma propagated into the host sediment in a non-brittle regime, through probably a hybrid process of viscous indentation and fluidization associated with mingling with the host sediment (Stephens et al., 2021).

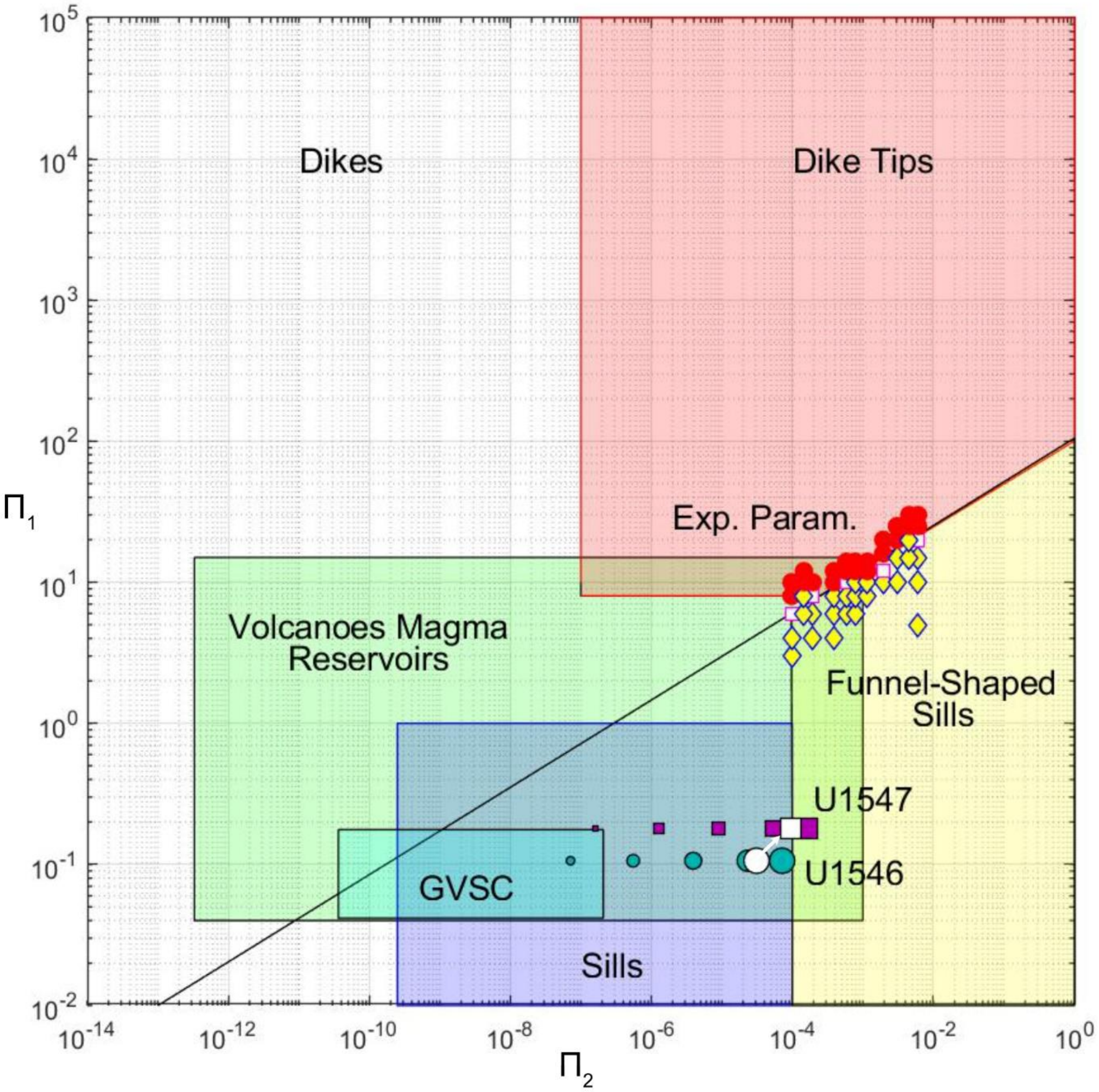

Figure 8. Graph modified after Galland et al. (2014) comparing parameters inferred from this study to characteristics geological values of $\Pi_1 = h/d$ and $\Pi_2 = \sigma_v/C$. Range of parameters tested for the flat sill U1546 cyan filled circles and magenta filled squares for the funnel-shaped sill U1547 (Tab. 5). Laboratory scaled experimental results forming dikes (red circles), hybrids (magenta squares), and cone sheets (yellow diamonds) are from Galland et al. (2014). Values for the fields: “dikes”, “dike tips”, “magma reservoirs” and “sills” are found in Galland et al. (2014). Typical values for “saucer-shaped sills” are derived from Galerne et al. (2008; 2010; 2011) based on studies of the Golden Valley Sill Complex (GVSC) in South Africa. The cone sheets field is extended after this study to lower values at least as low as the volcanic magma reservoirs field along Π_1 and to the upper limit of the sills field along the parameter Π_2.

Table 5: Summary of petrophysical parameters associated with the sill emplacement at Sites U1546 and U1547. For visual plotting refers to Fig. 8.

Meaning	**Symbol**	**U1546 (Ref. U1545)**	**U1547 (Ref. U1548)**	**Units**
Overburden thickness	*h*	245	155	m

Diameter of intrusion	d	2400	870	m
Magma viscosity	η	$1\text{x}10^2$–$1\text{x}10^6$		Pa.s
Magma velocity	V	$5\text{x}10^{-3}$–$5\text{x}10^{-2}$		m/s
Host cohesive strength	C	35000	35000	Pa
Cohesive Force	CF	80500	60000	Pa
Π_1	h/d	0.1021	0.1784	n.d
Π_2(C)	$\eta.V/(d.C)$	$0.07\text{x}10^{-6}$–$0.07\text{x}10^{-3}$	$0.16\text{x}10^{-6}$–$0.16\text{x}10^{-3}$	n.d
Π_2(CF)	$\eta.V/(d.CF)$	$3.11\text{x}10^{-5}$	$9.59\text{x}10^{-5}$	n.d

5.2. Evidence of host sediment assimilation

The result of the above petrophysical analysis suggests that the magma was emplaced with a combination of relatively low velocity and high viscosity (i.e., $V = 1\text{x}10^{-2}$ m/s, $\eta = 1\text{x}10^6$ Pa.s) leading to a high Π_2 value (Tab. 5; Fig. 8). Yet, results of the whole-rock analyses yield typical mafic rock compositions that correspond to viscosity values four to five orders of magnitude lower (10 and 100 Pa.s; e.g., Marsh 2002). These values considered for the above Ringvent sill suggest either a higher silica content or a higher crystallinity which would correspond to an advanced stage of cooling and crystallization.

Whole-rock geochemical compositions of both flat and funnel-shaped sills rule out a high silica content (Teske et al., 2021c,d). This probably means that the high water content of the unconsolidated host sediment played a major role in increasing the viscosity of the magma upon emplacement. The flat sill at Site U1546 emplaced just above the opal-A/CT transition (Fig. 2; Cheviet et al., 2023), while the funnel-shaped sill at Site U1547 emplaced ~90 m shallower (considering the top contact). Sediment assimilation has been unequivocally shown at Site U1546, with sediment clasts observed near the base of the sill (Cheviet et al., 2023). The presence of hornblende also shows clear evidence of massive water uptake by the sill at Site U1546 consistent with sediment assimilation during emplacement (SI-6). Although less evident from the textural analysis alone, thin section scans (SI-6) show that sediment and water uptake was similar if not greater at Site U1547 (i.e. 10% more water content than those corresponding to the depth of emplacement of the flat sill from Site U1546). In addition, the estimated volume of the funnel-shaped sill is seven times smaller than that of the flat sill at Site U1546 (SI-7). At the same time, a funnel-shaped geometry facilitates the upwelling of hydrothermal fluids (which would otherwise be trapped underneath a flat sill; e.g. Galerne and Hasenclever, 2019) and hence results in more efficient cooling by hydrothermal circulation. We therefore suggest that the funnel-shaped sill at Site U1547 has cooled and crystallized faster than the flat sill at Site U1546. This explains the more uniform fined-grained texture found throughout the Ringvent sill (section 4.3, and SI-6).

Quantitative micro-CT analysis shows that the higher porosity of the Ringvent sill is related to the presence of half-centimeter large vesicles accounting for nearly 10% of the bulk porosity in instrument range. By reconstituting the initial porosity attributed to large vesicles prior to carbonate precipitation, we estimate that the bulk porosity of the Ringvent sill might have been as large as 10 to 20%. We attribute the formation of these large vesicles and related textures to a process of assimilation of wet sediment during emplacement. Whereas water is relatively easily absorbed and diffused in the basaltic magma, thermogenic gas mobilized by almost instantaneous thermal cracking during assimilation remains exsolved and eventually nucleates vesicles (Pistone et al., 2020; see SI-2 for further support and Figs. SI-1-2 & 3). We note here that this process should have applied to the deeper sill at Site U1546, since the host sediments have similar bulk TOC content of 2 wt.% (Teske et al., 2021a). A closer inspection of the top sill margin sample (46-7, Tab. SI-1-1, Fig. 3) indicates that vesicles filled with clay minerals are present (see also SI-6, Fig. SI-6-1). The lower abundance of these vesicles at the Site U1546 sill, although surprising, could be attributed to the 90 m depth difference between the two sills at time of emplacement, and a faster cooling rate of the Ringvent funnel-shaped sill.

Analyses of the initial vesicle shapes (Ringvent sill) after removing carbonate mineralization indicate a high sphericity (Fig. SI-7-2). This suggests that the gas bubbles were unable to move and deform, also being indicative of a relatively high viscosity of the magma despite the relatively fine-grained matrix. This places the temperature of the magma body at near-solidus temperature shortly after its emplacement. With an initial intrinsic porosity up to 10–20%, there is no doubt that the Ringvent sill is highly porous and permeable. Porosity and permeability in cooling magma opens a percolation pathway to surrounding fluid flow as soon as the magmatic body enters the brittle regime marked by the solidus temperature (Lenhardt et al., 2023; Rabbel et al., 2023). However, in a standard cooling process, the development of porosity and permeability inside the magma is characterized by the formation of columnar joints that have a porosity up to 20% in the fracture planes (e.g., Lamur et al., 2017; 2018). With a porosity up to 20% in the bulk of the magma itself, the magma may have cooled more rapidly as it opened to epithermal fluid flow (similar to Jurassic sills from the Karoo Basin, South Africa; i.e., Lenhardt et al., 2023). This conclusion is consistent with the fact that the extent of contact aureole process is already limited in the flat sill documented at Site U1546. As demonstrated by Lizarralde et al. (2023), the thin contact aureole thickness (only ~20% of the sill thickness) implies that less thermogenic gas is mobilized by the contact metamorphism process. Here we show that the limited extent of the contact aureole thickness might be attributed to a relatively low temperature of the magma body once its emplacement stopped and it started to cool and crystallized. This process took place in addition to the process identified by Lizarralde et al. (2023) who pointed out that high porosity and water content of the host sediment would have also favored an efficient cooling by hydrothermal fluid flow thereby limiting the extent of the contact aureole.

5.3. Geological model of magma emplacement in unconsolidated sediments

Four observations suggest that the Ringvent sill cooled very quickly: (1) The funnel shape of the sill favors epithermal fluid flow along its inclined contacts; (2) magma-sediment mingling and assimilation of wet unconsolidated sediment bring down the bulk temperature of the magmatic body and hence limit the extent of heat transfer to the host sediment; (3) the high porosity of the host sediment facilitates the supply of water and heat dissipation through convection; and (4) the permeability of the sill increased greatly after solidification when columnar jointing developed (e.g. Lamur et al., 2018) and allowed circulating fluids to enter the cooling sill (e.g. Rabbel et al., 2023). Thus, the sill became part of the domain affected by epithermal fluid flow which until then was restricted to the surrounding host sediment.

The effect of permeability and porosity development within igneous sills, during cooling and crystallization, has been numerically simulated by Rabbel et al. (2023). Their numerical model results showed that fluid flow patterns were completely re-organized in the aftermath of the formation of the cooling joints. Similar to what we suggest for the Ringvent sill, jointing facilitated hydrothermal circulation of fluids through the sill, which increased the cooling rate.

Using the sill at Site U1546 as a reference, and the information that the fluid flow circulating inside the funnel-shaped intrusion has acquired an isotopic signature typical of fluid flow percolating through basalt, we can now propose a mechanical model of sill emplacement in shallow wet unconsolidated sediment (Fig. 9).

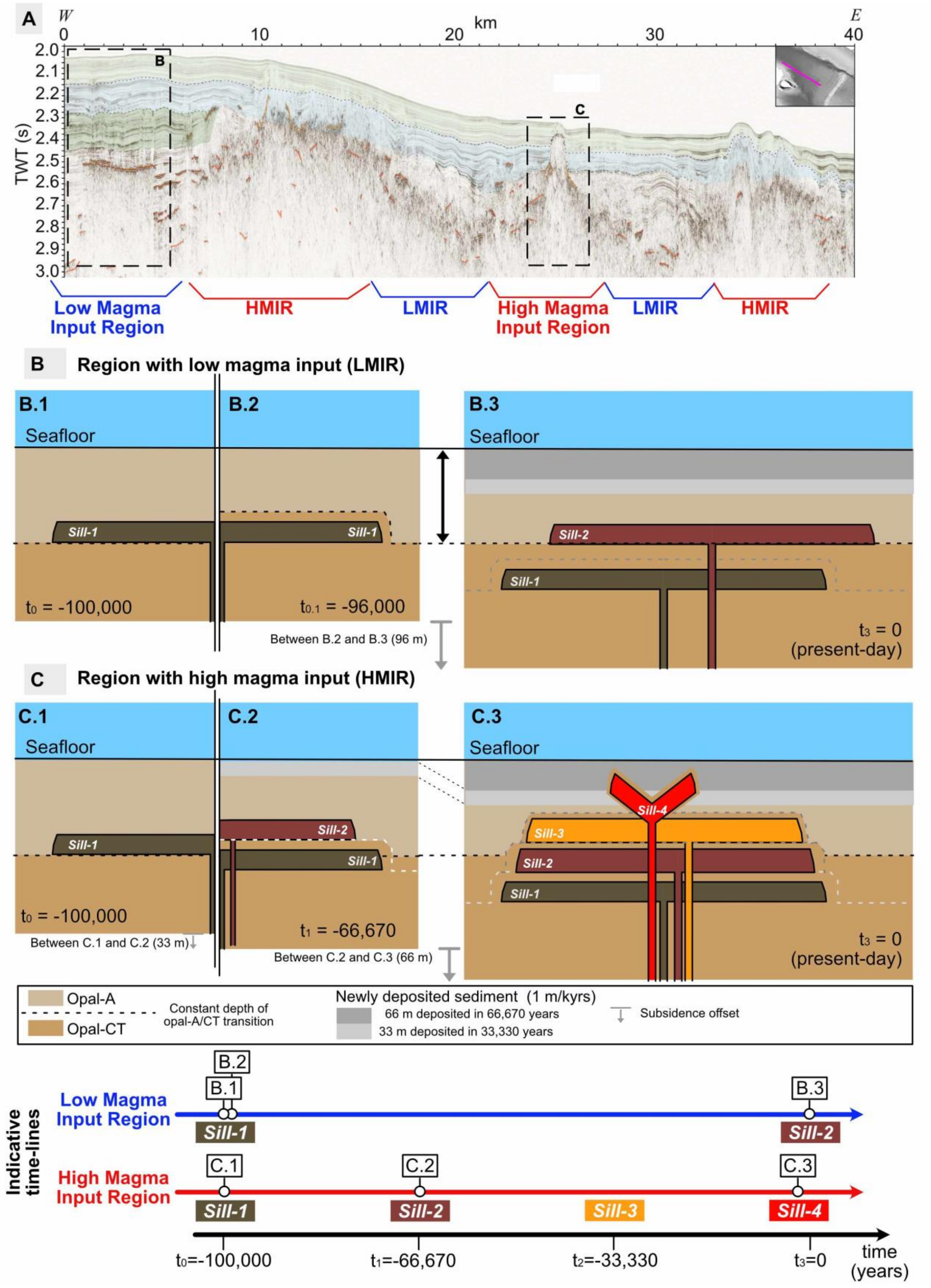

Figure 9. Geological model of sill emplacement in the top wet unconsolidated sediment of the Guaymas Basin. A. Northwest to southeast seismic profile (SO-118) showing the paired IODP X385 Sites U1545 and U1546 (B) as well as U1547 and U1548 (C). Detailed conceptual model of magma emplacement in Low Magma Input Region (LMIR; B) and High Magma Input Region (HMIR; C) with both a rheological depth control dictating the

transition from a vertical magma propagation to a horizontal magma propagation (i.e., the transition from siliceous claystone to diatom ooze). A comparative timeline of both LMIR and HMIR is provided.

The model proposed here highlights possible large-scale effects of alternating regions with low magma input (LMIRegion), and high magma input (HMIRegion) that corresponds to a higher frequency of magma intrusion events (Fig. 9). The rheological control of the opal-A/CT transition acts as a depth focus for locating the transition from a vertical to a horizontal mode of magma propagation (Fig. 9B). Because the opal-A/CT transition is controlled by temperature, the fundamental effect of contact metamorphism process is that it causes opal-A to transform into opal-CT and quartz around and above the newly emplaced sill, thereby shallowing the opal-A/CT transition locally (e.g., Fig. 9B.2). Two end-member cases can be found in this configuration. Hereafter, we consider low- and high- magma input in terms of rate compared to the time it takes for sedimentation and subsidence to overcome the local shoaling of the opal-A/CT transition. In low-magma input regions (LMIR), sills always intrude at a constant distance from the seafloor, i.e., just above the opal-A/CT transition (Fig. 9B.3). This scenario assumes that over time the local geothermal gradient and sedimentation rates do not vary (Aiello et al., 2024), thereby maintaining the opal-A/CT transition at a constant subseafloor depth (Fig. 9B,C). In high-magma input regions (HMIR; compared to sedimentation and subsidence), flat sills are emplaced one after the other, increasingly shoaling the opal-A/CT transition to a point where the free surface effect of the nearby seafloor dictates the magma to change from a vertical dike to a funnel-shaped geometry, instead of a flat sill (Fig. 9C.3). According to our estimates three flat sills could have emplaced one after another before the most recent intrusion met the parameter requirement to form a shallow funnel-shaped intrusion (Fig. 9C.3). This model suggests that frequent intrusions of flat sills stacking upward are fundamental to the development of the funnel-shape sill geometry at Ringvent. The present model substantiates and refines what had been suggested by earlier, DSDP-related research on the Guaymas Basin (Einsele et al., 1980; Einsele 1982; 1985).

The suggestion that the flat sill at Site U1546 represents an example of LMIR and the Ringvent funnel-shaped sill (U1547) represents an example of HMIR is supported by textural differences between the rocks forming the compared sills. Dolerite rock from Site U1546 contains large plagioclase phenocrysts that cannot be found in the phyric to aphyric rocks of the Ringvent sill (SI-5; Teske et al., 2021c). This suggests that magma reservoirs feeding sills in LMIR have time to grow larger crystals that are sampled by ascending magma during dyking events.

5.4. Present-day hydrothermal fluid flow state

The hydrothermal history of the Ringvent sills can be divided into two main periods. The first one is a high-temperature regime associated with early cooling and initiation of jointing that boosted permeability. This high-temperature regime would have been relatively short-lived. Given the weak rheological nature of the host sediment and its high porosity and water content, temperature in direct contact with the Ringvent sill is likely to have dropped to <100°C within the first 1,000 years after emplacement (estimates based on simple heat conduction cooling model, e.g., Aarnes et al., 2010). During this period, high-permeability fluid flow pathways, formed by localized high-temperature fluid flow advection constitute a ring of vents that root to the upper rim of the Ringvent sill. Following a descending temperature path and considering the composition of the host sediment, a single vent structure is expected to be made up of sulfides, sulfates (e.g., barite), and calcite, concluding with lower-temperature deposition of amorphous silica (Teske et al., 2019).

The simplest physical explanation for the current state of the Ringvent sill hydrothermal system is that the highly porous and permeable magma plumbing system taps into deeply sourced hot fluids. Using Holes U1548D and E as reference geothermal gradient, and assuming an adiabatic ascent through the magma plumbing system, we estimate that fluids may have come from as deep as 325 mbsf (Fig. 7C). This depth is significantly below the inferred base of the Ringvent sill (maximum depth ~250 mbsf, Fig. 7A). This model explains the relatively mild seafloor venting temperature without having to invoke a waning heat source associated with magma cooling. But more importantly, it implies that fluid will rise first through the vertical feeder before it starts to percolate inside the funnel-shaped sill. We can thus expect that the degree of interaction with the host subvolcanic system will be more significant as fluids flow in through the funnel-shaped sill. This model is consistent with our temperature-derived model from oxygen isotope measured on precipitated calcite. It indicates higher temperature just above the assumed location of the vertical magma feeder to the Ringvent sill (Fig. 7C). At the top interface of the sill with the relatively more impermeable sediment, hot fluids are guided outwards towards the shallowest part of the sill. At this point the high-permeability pathway is probably relayed by the root of the hydrothermal vent pipes formed at high-temperature during emplacement and cooling of the sill (Fig. 7C). The cooler temperature signal derived from oxygen isotope on carbonate just outside the center of the sill is consistent with a local convection cell driven by the hot fluid upwelling from deeper levels.

6. Summary and Conclusions

We integrate 2D seismic and IODP X385 data to provide insights into the mechanics of magma emplacement into the top unconsolidated sediment of the Guaymas young rift basin (Gulf of California, Mexico). Petrographic and textural analysis by petrophysical methods and advanced imagery (Micro-CT) are complemented by stable isotope geochemistry of carbonate precipitates in voids of the uppermost sill parts. Temperatures derived from oxygen isotope composition are compare with in-situ measurement from the IODP X385 to infer the state of the Ringvent hydrothermal system.

Our results show that magma emplacement in the shallow unconsolidated sediment is controlled by the weak rheology of the host sediments, which leads to the formation of flat sill at depth, as soon as the ascending magma enters the top unconsolidated sediments. Magma emplaces just above the upper limit of the top cemented lithology to form flat sills. This general mechanism for depth control on sill emplacement is marked in the Guaymas Basin by the silica-rich sediment transforming from opal-A into opal-CT and quartz.

Regional variations in magma flux also affect the style of sill emplacement. In regions of low magma input, sills will always form above the opal-A/CT transition and emplace at constant ~325 m depth from the seafloor. In regions where the rate of magmatism is high and frequent, contact metamorphism drives successive sill emplacement in a runaway towards the basin top. The funnel-shaped sill at the Ringvent site represents the intrusion topping a stacked sequence of sill intrusions. Site U1546 represents a region of relatively less frequent magma input (every 100,000 years), while Sites U1547/U1548 represents a location of frequent magma input (every 33,000 years). In the latter case, where the magma input outpaces subsidence and sedimentation, successive sill intrusions stack on top of each other to eventually reach the shallow subseafloor. This mechanism could form the root system of a future seamount (e.g Medialdea et al., 2017).

The change in shape from a flat sill to a funnel-shape intrusion is governed by complex interplays of magma with water and sediment. Magma/sediment mingling is expected to increase viscosity (due to cooling) and, thus, lower the magma ascent velocity in the conduit. The weak host sediments affect magma propagation through a combination of viscous-indenter, mingling, assimilation, and digestion, processes that all contribute to an efficient space accommodation. The transition from a vertical dike to a directly transgressive inverted cone (i.e., funnel-shape), instead of a flat sill, is controlled by the ratio of the viscous stress and cohesive strength of the host sediment.

Our petrographic and textural analyses strongly support the idea that magma-sediment mingling is one of the prominent processes occurring upon emplacement. This process has a strong impact of the final petrophysical and hydraulic properties of the crystallized magma. Above all, we found that the assimilation of unconsolidated sediment rich in water and organic matter ultimately leads to the formation of significant porosity of the doleritic hypabyssal rock (up to 20%). The mingling of organic-rich sediment boosts the development of a very large porosity and permeability within the top funnel-shaped sill. The magma plumbing system can then become a conduit for hydrothermal fluids that can be sourced from underneath the stacked pile of sills. This fundamentally transforms the stacked-sill plumbing system into a hydraulic bypass of the low-permeability unconsolidated surrounding sediments, promoting the ascent of hot fluids that feed the seafloor hydrothermal field at Ringvent (Site 1547). The current temperature of the venting fluids at Ringvent coincides with temperatures estimated from oxygen isotopes for calcite formation within the Ringvent sill, suggesting that fluids actively venting are deeply sourced (~250−325 mbsf) and rise adiabatically to the seafloor. The Ringvent site hence appears to be a steady subseafloor incubator, where high metabolic energy availability and tolerable temperatures (≤90°C) enable microbial organisms to thrive.

We conclude that magma/sediment mingling upon sill emplacement is a key process at Ringvent. Frozen remains of such mingling are known in geology under the term peperites that comprise multitudes of geological facies based on often million years old exhumed systems. We characterize here, for the first time, active processes associated with this fundamental geological process. It is anticipated that our research will enable researchers to revisit fossil systems and better understand their significance. Our results fertilize such efforts as we now can relate a centimeter-scale peperite facies to the magmatic body shape they belong to and provide physical understanding for further quantitative investigations on carbon trap and/or release at the seafloor, in young rift basins.

Our study refines the role of magmatism in organic-rich basins and its control on the carbon cycle. Two distinct scenarios can be described. When magma emplaces deep in sedimentary rocks, contact metamorphism leads to sudden degassing of massive amount of thermogenic gas through short-lived high-temperature hydrothermal systems. In contrast, magma emplacement at shallow depth in unconsolidated sediment leads to little thermogenic gas produced from thin contact aureoles, but promote long-lasting, low-temperature hydrothermal fluid flow pathway, that promote efficient young-rift-basin degassing of diagenetically produced thermogenic gas.

We expect similar processes to operate and be found in sedimented ridges (e.g. Escanaba trough), back-arc spreading centers (e.g. Lau Basin), ridge flanks (e.g. abyssal plane off the Canary Islands), and more generally every early rift system leading to ocean basin formation (e.g., Afar-Red sea transition) is susceptible to host such a system. Additionally, these sill plumbing systems might be the root of many intraplate volcanic seamounts and islands. Abundant, sediment-hosted hydrothermal systems during opening of oceans may have boosted diversity and richness of microbial communities in periods dominated by continental breakup.

Open Research

Supporting Information SI, includes eight text sections, that are supplied with a total of thirteen Figures, four Tables, and three equations.

ACKNOWLEDGMENTS

This research used samples and data provided by the International Ocean Discovery Program (IODP). Funding for this research was provided by the German Research Foundation (DFG) funding priority program SPP 527. Project number 447431016 is led by Christophe Galerne at the University of

Bremen. The Bundesanstalt für Geowissenschaften un Rohstoffe (BGR) and ECCORD provided funds for sailing. Shipboard data presented here is accessible online (www.iodp.org/access-data-and-sample). We sincerely thank the IODP technical staff and the R/V *JOIDES Resolution* crew for their invaluable assistance. We thank members of the science party of IODP X385 that are not directly involved with this research for their invaluable shipboard contributions. We also thank the entire staff of the R/V *JOIDES Resolution* for their flawless technical support, and our outstanding outreach officer and science journalist Rodrigo Pérez Ortega.

REFERENCES CITED

Aarnes, I., Svensen, H., Connolly, J.A.D., and Podladchikov, Y.Y., 2010. How contact metamorphism can trigger global climate changes: Modeling gas generation around igneous sills in sedimentary basins. Geochimica et Cosmochimica Acta, 74(24), 7179-7195. http://doi.org/10.1016/j.gca.2010.09.011

Bailey, C.B., Clough, C.T., Wright, W.B., Ritchey J.E., and Wilson, G.V., 1924. Tertiary and Post-Tertiary geology of Mull, Loch Aline and Oban. Memoirs of the Geological Survey of Scotland. Edinburgh: H. M. Stationery Office, 120 George St., pp. 445.

Aiello, I., Höfig, T.W., Ribouleau, A., Galerne, C., and Buatier, M., 2022. Relationships between routing of magma and biosilica diagenesis in the shallow subseafloor of a nascent ocean basin (Guaymas Basin, Gulf of California). EGU General Assembly 2022, https:/doi.org/10.5194/egusphere.egu22-6464

Aiello, I., Höfig, T.W., Ribouleau, A., Teske, A., Lizarralde, D., and the IODP Exp 385 scientists, 2024. Mineralization kinetics of biosiliceous sediments in hot subseafloor. Geochimica et Cosmochimica Acta 380, p. 71-82. https://doi.org/10.1016/j.gca.2024.07.005

Berndt, C. et al., 2015, SO241-MAKS: Magmatism induced carbon escape from marine sediments, RV SONNE 241 Cruise Report, http://doi.org/10.3289/CR_S241

Berndt, C., et al., 2016, Rifting under steam – How rift magmatism triggers methane venting from sedimentary basins: Geology, 44, 767-770. http://doi.org/10.1130/G38049.1

Cheviet, A., Buatier, M., Choulet, F., Galerne, C., Ribouleau, A., Aiello, I., Marsagia, K., and Höfig, T.W., 2023. Contact metamorphism reactions and fluid-rock interactions related to magmatic sill intrusion in the Guaymas Basin. European Journal of Mineralogy. 35, 987-1007. https://doi.org/10.5194/ejm-35-987-2023

Einsele, G., Gieskes, J.M., Curray, J., Moore, D.G., et al., 1980. Intrusion of basaltic sills into highly porous sediments, and resulting hydrothermal activity. Nature, Vol. 283, p. 441-445. https://doi.org/10.1038/283441a0

Einsele, G., 1982. Mechanism of sill intrusion into soft sediment and expulsion of pore water. In: Curray, J.R., Moore D.G. et al., Initial reports of the Deep Sea Drilling Project, Volume 64, Part 2: Washington, D.C., U.S. Government Printing Office, p. 1169-1176.

Einsele, G., 1985. Basaltic sill-sediment complexes in young spreading centers: Genesis and significance. Geology, Vol. 13, p. 249-252. https://doi.org/10.1130/0091-7613(1985)13<249:BSCIYS>2.0.CO;2

Friedmann I., and O'Neil, J.R., 1977. Compilation of stable isotope fractionation factors of geochemical interest. U.S. Geological Survey Professional Paper 440-KK, Data of Geochemistry, 6th Edition, Chapter KK, KK1-KK12. https://doi.org/10.3133/pp440KK

Galerne, C.Y., Caroff, M. Rolet J., Le Gall, B., 2006, Magma-sediment mingling in an Ordovician rift basin: The Plouézec-Plourivo half-graben, Armorican Massif, France: Journal of Volcanology and Geothermal Research, v. 155, p. 164-178. https://doi.org/10.1016/j.jvolgeores.2006.03.030

Galerne, C.Y., Neumann, E.-R., Planke, S., 2008, Emplacement Mechanisms of Sill Complexes: Information from the Geochemical Architecture of the Golden Valley Sill Complex, South Africa: Journal of Volcanology and Geothermal Research, v. 177, p. 425-440. https://doi.org/10.1016/j.jvolgeores.2008.06.004

Galerne, C.Y., Neumann, E.-R., Aarnes, I., Planke, S., 2010. Magmatic Differentiation Processes in Saucer-Shaped Sills: Evidence from the Golden Valley Sill in the Karoo Basin, South Africa. *Geosphere*, v. 6, p. 163-188. https://doi.org/10.1130/GES00500.1

Galerne, C.Y., Galland O., Neumann, E.-R., Planke, S., 2011, 3D relationships between sills and their feeders: evidence from geological data, geochemistry and experimental modelling. Journal of Volcanology and Geothermal Research, v. 202, p. 189-199. https://doi.org/10.1016/j.jvolgeores.2011.02.006

Galland, O., Planke, S., Neumann, E.-R., Malthe-Sørenssen, A., 2009, Experimental modelling of shallow magma emplacement: Application to saucer-shaped intrusions. Earth and Planetary Science Letters, v. 277, p. 373-383. https://doi.org/10.1016/j.epsl.2008.11.003

Galland, O., Burchardt, S., Hallot, E., Mourgues, R., and Bulois, C., 2014. Dynamics of dikes versus cone sheets in volcanic systems. Journal of Geophysical Research: Solid Earth, 119, 6178-61192, https://doi.org/10.1002/2014JB011059

Galland, O., Holohan, E., Van Wyk de Vries, B., and Burchardt, S., 2018. Laboratory Modelling of Volcano Plumbing Systems: A Review. **In:** Breitkreuz, C., Rocchi, S. (eds) Physical Geology of Shallow Magmatic Systems. Advances in Volcanology. https://doi.org/10.1007/11157_2015_9

Galland, O., and Scheibert, J., 2013. Analytical model of surface uplift above axisymmetric flat-laying magma intrusions: Implications for sill emplacement and geodesy. Journal of Volcanology and Geothermal Research 253, 114-130. https://doi.org/10.1016/j.jvolgeores.2012.12.006

Hajime, Y., 1967. Relationship between soil cohesion and sear strength. Soil Science and Plant Nutrition, Vol. 14, No. 3.

Hansen, D.M., and Cartwright, J., 2006. The three-dimensional geometry and growth of forced folds above saucer-shaped igneous sills. Journal of Structural Geology, 28, 1520-1535. https://doi.org/10.1016/j.jsg.2006.04.004

Haug Ø.T., Galland, O., Souloumiac, P., Souche, A., Guldstrand, F., Schmiedel, T., and Maillot, B., 2018. Shear Versus Tensile Failure Mechanisms Induced by Sill Intrusions: Implications for Emplacement of Conical and Shear-Shaped Intrusions. Journal of Geophysical Research: Solid Earth, 123, 3430-3449. https://doi.org/10.1002/2017JB015196

Heuer, V., et al., 2020. Temperature limits to deep subseafloor life in the Nankai Trough subduction zone. Science, Volume 370, Issue 6521, https://doi.org/10.1126/science.abd7934

Jamtveit, B., Svensen, H., Podladchikov, Y.Y., and Planke, S., 2004, Hydrothermal vent complexes associated with sill intrusions in sedimentary basins. In: Breitkreuz, C., Petford, N., (Eds). Physical Geology of High-Level Magmatic Systems. Geological Society, London, Special Publicaitons, v. 234, p. 233-241. 0305-8719/04/$15.00. https://doi.org/10.1144/GSL.SP.2004.234.01.15

Kjoberg, S., T. Schmiedel, S. Planke, H. Svensen, J. Millett, D. A. Jerram, O. Galland, I. Lecomte, N. Schofield, and A. Heslem, 2017, 3D structure and formation of hydrothermal vent complexes at the Paleocene-Eocene transition, the Møre Basin, mid-Norwegian Margin. Interpretation, 5(3), SK65-SK81, https://doi.org/10.1190/int-2016-0159.1

Lamur, A., Kendrick, J.E., Eggertsson, G.H., Wall, R.J., Ashworth, J.D., and Lavallée, Y., 2017. The permeability of fractured rocks in pressurised volcanic and geothermal systems. Scientific Reports, 7:6173, https://doi.org/10.1038/s41598-017-05460-4

Lamur, A., Lavallée, Y., Iddon, F., Hornby, A., Kendirck, J.E., von Aulock, F.W., and Wadsworth, F.B., 2018. Discolosing the temperature of columnar joiting in lavas. Nature Communications, (2018)9:1432, https://doi.org/10.1038/s41467-018-03842-4

Lenhardt, N., Galerne, C., Le Roux, P., Götz, A.E., Lötter, F.J.P. 2023 Geochemistry of dolerite intrusions of the southeastern Main Karoo Basin, South Africa: Magma evolution, evidence for thermogenic gas sequestration, and potential implications for the early Toarcian oceanic anoxic event. Gondwana Research *113, 144-162*, https://doi.org/10.1016/j.gr.2022.10.017

Lizarralde, D., Axen, G.J., Brown, H.E., Fltecher, J.M., Gonzalez-Fernandez, A., Harding, A.J., Holbrook, W.S., et al., 2007. Variation in styles of rifting in the Gulf of California. Nature, 448(7152): 466-469, https://doi.org/10.1038/nature06035

Lizarralde, D., Soule, S.A., Seewald, J.S., and Proskourowski, G., 2011. Carbon release by off-axis magmatism in a young sedimented spreading centre. Nature Geoscience, 4:50-54, https://doi.org/10.1038/ngeo1006

Lizarralde, D., Teske, A., Höfig, T.W., González-Fernández, A., and the IODP Expedition 385 Scientists. 2023. Carbon released by sill intrusion into young sediments measured through scientific drilling. Geology 51(4):329-333. https://doi.org/10.1130/G50665.1

Neumann, F., Negrete-Aranda, R., Harris, R., Contreras, J., Galerne, C.Y., Peña-Salinas, M., Spelz, R., Teske, A., Lizarralde, D., Höfig, T.W., 2023, Heat Flow and Thermal Regime in the Guaymas Basin, Gulf of California: Estimates of Conductive and Advective Heat Transport. Basin Research. https://doi.org/10.1111/bre.12755

Marty, B., and Jambon, A., 1987. C^3 He in volatile fluxes from the solid Earth: implications for carbon geodynamics. Earth and Planetary Science Letters, 83, 16-26, https://doi.org/10.1016/0012-821X(87)90047-1

Mathieu, L., Van Wyk de Vries, B., Holohan, E.P., and Troll, V.R., 2008. Dykes, cups, saucers and sills: Analogue experiments on magma intrusion into brittle rocks. Earth and Planetary Science Letters, 271(1-4), 1-13. https://doi.org/10.1016/j.epsl.2008.02.020

Medialdea T., Somoza, L., Gonzalez, F.J., Vazquez J.T., de Ignacio, C., Sumino, H., Sanchez-Guillamon, O., Orihashi, Y., León R., Palomino, D., 2017. Evidence of a modern deep water magmatic hydrothermal system in the Canary Basin (eastern central Atlantic Ocean). Geochemistry, Geophysics, Geosystems, Vol. 18(8), p. 3138-3164. https://doi.org/10.1002/2017GC006889

Merle, O., and Donnadieu, F., 2000. Indentation of volcanic edifices by the ascending magma. In B. Vendeville, Y. Mart, & J.-L. Vingneresse (Eds.), Salt, shale and igneous diapirs in and around Europe (Vol. 174, pp. 43-53). Geological Society, London, Special Publications. https://doi.org/10.1144/GSL.SP.1999.174.01.03

Marsh, B.D., 2002. On bimodal differentiation by solidification front instability in basaltic magmas, part 1: Basic mechanics. Geochimica et Cosmochimica Acta, Vol. 66, No. 12, pp. 2211-2229. https://doi.org/10.1016/S0016-7037(02)00905-5

O’Neil, J.R., Clayton, R.N., Mayeda, T.K., 1969. Oxygen isotope fractionation in divalent metal carbonates. The Journal of Chemical Physics, 51, 5547-5558, https://doi.org/10.1063/1.1671982

Peter, J.M., and Shanks III, W.C., 1992. Sulfur, carbon, and Oxygen isotope variations in submarine hydrothermal deposits of Guaymas Basin, Gulf of California. Geochimica et Cosmochimica Acta, Vol., 56, pp. 2025-2040. https://doi.org/10.1016/0016-7037(92)90327-F

Persad, L.D., and Marsaglia, K.M., 2023. Data report: detailed lithologic columns for IODP Expedition 385 and DSDP Leg 64 sites in the Guaymas Basin, Gulf of California, Mexico. In Teske, A., Lizarralde, D., Höfig, T.W., and the Expedition 385 Scientists, Guaymas Basin Tectonics and Biosphere. Proceedings of the International Ocean Discovery Program, 385: College Station, TX (International Ocean Discovery Program). https://doi.org/10.14379/iodp.proc.385.202.2023

Philipps, W.J., 1974. The dynamic emplacement of cone sheets. Tectonophysics, 24, Issues 1-2, 69-84. https://doi.org/10.1016/0040-1951(74)90130-9

Pistone, M., Caricchi, L., and Ulmer, P., 2020. CO2 favours the accumulation of excess fluids in felsic magmas. Terra Nova. Vol., 33(2). https://doi.org/10.1111/ter.12496

Rabbel, O., Hasenclever, Galerne, C., J., Galland, O., Mair, K., Palma, O., 2023. Impact of permeability evolution in igneous sills on hydrothermal flow and hydrocarbon transport in volcanic sedimentary basins. Solid Earth, 14, 625-646, https://doi.org/10.5194/se-14-625-2023

Sarkar, S., Moser, M., Berndt, C., Doll, M., Böttner, C., Chi, W.-C-. Klaeschen, D., Galerne, C., Karstens, J., Geilert, S., Mortera-Gutierrez, C., and Hensen, C., 2022. Thermal state of the Guaymas Basin derived from gas hydrate bottom simulating reflections and heat flow measurements. Journal of Geophysical Research: Solid Earth, 127, e202JB023909. https://doi.org/10.1029/2021JB023909

Schmiedel, T., Kjoberg, S., Planke, S., Magee, C., Galland, O., Schofield, N., Jackson, C.A.-L., and Jerram, D.A., 2017. Mechanisms of overburden deformation associated with the emplacement of the Tulipan sill, mid-Norwegian margin. Interpretation, Vol. 5(3). https://doi.org/10.1190/INT-2016-0155.1

Skilling, I.P., White, J.L., and McPhie J., 2002. Peperite: Processes and Products of Magma-Sediment Mingling. Journal of Volcanology and Geothermal Research, Vol. 114, Issues 1-2, https://doi.org/10.1016/S0377-0273(01)00278-5

Spacapan J.B., Galland, O., Leanza, H.A., and Planke, S., 2016, Igneous sill finger emplacement mechanism in shale-dominated formations: a field study at Cuesta del Chihuido, Neuquén Basin, Argentina: Journal of the Geological Society. https://doi.org/10.1144/jgs2016-056

Stephens, T., Walker, R., Healy, D., and Bubeck, A., 2021. Segment tip geometry of sheet intrusions, II: Field observations of tip geometries and a model for evolving emplacement mechanisms. Volcanica, 4(2), pp. 203-225. https://doi.org/10.30909/vol.04.02.203225

Svensen, H., Planke, S., Malthe-Sørenssen, A., Jamtveit, B., Myklebust, R., Eidem, T.R., Rey, S.S., 2004, Release of methane from a volcanic basin as a mechanism for initial Eocene global warming: Nature, 429(6991): 542-545. https://doi.org/10.1038/nature02566

Teske, A., de Beer, D., McKay L.J., Tivey M.K., Biddle J.F., Hoer, D., Lloyd, KG., Lever, M.A., Røy, H., Albert, D.B., Mendlovitz, H.P., and McGregor, B.J. 2016, The Guaymas Basin Hiking Guide to Hydrothermal Mounds, Chimneys, and Microbial Mats: Complex Seafloor Expressions of Subsurface Hydrothermal Circulation: Frontier in Microbiology 7:75, https://doi.org/10.3389/fmicb.2016.00075

Teske, A., McKay, L.J., Ravelo, A.C., Aiello, I., Mortera, C., Núñez-Useche, F., Canet, C., et al., 2019, Characteristics and evolution of sill-driven off-axis hydrothermalism in Guaymas Basin – the Ringvent site. Scientific Reports, 9(1):13847. https://doi.org/10.1038/s41598-019-50200-5

Teske, A., Lizarralde, D., Höfig, T.W., and the Expedition 385 Scientists, 2021a, Expedition 385 Summary, *in* Teske, A., et al., eds., Proceedings of the International Ocean Discovery Program, Expedition Reports, 385: College Station, Texas, International Ocean Discovery Program, https://doi.org/10.14379/iodp.proc.385.101.2021

Teske A, Lizarralde D, Höfig TW, and the Expedition 385 Scientists, 2021b. Site U1545, *in* Teske, A., et al., eds., Proceedings of the International Ocean Discovery Program, Expedition Reports, 385: College Station, Texas, International Ocean Discovery Program, https://doi.org/10.14379/iodp.proc.385.103.2021

Teske A, Lizarralde D, Höfig TW, and the Expedition 385 Scientists, 2021c: Site U1546, *in* Teske, A., et al., eds., Proceedings of the International Ocean Discovery Program, Expedition Reports, 385: College Station, Texas, International Ocean Discovery Program, https://doi.org/10.14379/iodp.proc.385.104.2021

Teske, A., Lizarralde, D., Höfig, T.W., and the Expedition 385 Scientists, 2021d, Site U1547 and U1548 *in* Teske, A., et al., eds., Proceedings of the International Ocean Discovery Program, Expedition Reports, 385: College Station, Texas, International Ocean Discovery Program, https://doi.org/10.14379/iodp.proc.385.105.2021

Teske, A., Lizarralde, D., Höfig, T.W., and the Expedition 385 Scientists, 2021e. Expedition 385 methods *in* Teske, A., et al., eds., Proceedings of the International Ocean Discovery Program, Expedition Reports, 385: College Station, Texas, International Ocean Discovery Program, https://doi.org/10.14379/iodp.proc.385.102.2021

Wohletz, K., 2002. Water/magma interaction: some theory and epxeriments on peperite formation. Journal of Volcanology and Geothermal Research, v. 114, Issues 1-2. p. 19-35. https://doi.org/10.1016/S0377-0273(01)00280-3

Zheng, Y.-F., and Hoefs J., 1993. Carbon and oxygen isotopic covariations in hydrothermal calcites – Theoretical modelling on mixing processes and application to Pb-Zn deposits in the Harz Mountains, Germany. Mineralium Deposita 28(2): 79-89. https://doi.org/10.1007/BF00196332

Zimanowski, B., and Büttner, R., 2002. Dynamic mingling of magma and liquefied sediments. Journal of Volcanology and Geothermal Research, v. 114, Issues 1-2. p. 37-44. https://doi.org/10.16/S0377-0273(01)00281-5